TURBULENT FLOW PAST OVER A 3–DIMENSIONAL TRIANGULAR BLUFF–BODY FLAMEHOLDER USING DIRECT NUMERICAL SIMULATIONS

By

Glenn Cooper Vidal Urquiza

A thesis submitted in partial fulfillment of the requirements for the degree of

MASTER OF SCIENCE

in

MECHANICAL ENGINEERING

UNIVERSITY OF PUERTO RICO
MAYAGÜEZ CAMPUS

May, 2008

Approved by:

R. Vikram Raja Pandya, Ph.D Member, Graduate Committee	Date
Gustavo Gutierrez, Ph.D Member, Graduate Committee	Date
Stefano Leonardi, Ph.D President, Graduate Committee	Date
Andrés Calderón, Ph.D Representative of Graduate Studies	Date
Paul Sundaram, Ph.D Chairperson of the Department	Date

Abstract of Dissertation Presented to the Graduate School
of the University of Puerto Rico in Partial Fulfillment of the
Requirements for the Degree of Master of Science

TURBULENT FLOW PAST OVER A 3–DIMENSIONAL TRIANGULAR BLUFF–BODY FLAMEHOLDER USING DIRECT NUMERICAL SIMULATIONS

By

Glenn Cooper Vidal Urquiza

May 2008

Chair: STEFANO LEONARDI
Major Department: Mechanical Engineering

In gas turbine combustion system, pollution emissions like CO and NO_x produce a hard impact on ecosystem. These emissions are due to combustion instability during which the flame undergoes rapid oscillations and eventually blows out completely. In gas turbine, flame stabilization is often achieved through the use of recirculation zone created by a bluff body usually called "flamehoder". A flame holder improves the mixing of hot combustion products with the incoming fuel and air mixture.

In the present study, a detailed bluff–body flameholder is studied. Direct Numerical Simulations (DNS) at low Reynolds number have been performed. Various quantities as mean velocities, turbulent fluctuations and static pressures are measured. Behind the flameholder the wake is similar to a Karman Vortex. The pressure distribution around the flame holder shows a high variability corresponding to the oscillation of the streamlines. Visualization of streamlines, pressure contours, rms of velocity are shown in this work.

Resumen de Disertación Presentado a Escuela Graduada
de la Universidad de Puerto Rico como requisito parcial de los
Requerimientos para el grado de Maestría en Ciencias

FLUJO TURBULENTO ALREDEDOR DE UN TRIDIMENSIONAL TRIANGULAR "BLUFF–BODY FLAMEHOLDER" USANDO "DIRECT NUMERICAL SIMULATIONS"

Por

Glenn Cooper Vidal Urquiza

Mayo 2008

Consejero: STEFANO LEONARDI
Departamento: Ingeniéria Mecańica

En los sistemas de combustión de las turbinas de gas, emisiones de contaminantes como CO y NO_x producen un duro impacto en el ecosistema. Estas emisiones son debido ha inestabilidad de la combustión, en la cual la flama sufre rápidas oscilaciones y eventualmente produce un completo soplado. En turbinas de gas, la estabilización de la flama es usualmente alcanzado a través de el uso de zonas de recirculación creadas por "bluff–body", usualmente llamado "flameholder". Flameholder mejora la mezcla de los calientes productos de combustión con la mezcla aire–combustible entrante.

En el presente estudio un detallado "bluff–body flameholder" es estudiado. "Direct Numerical Simulation" (DNS) para bajos Numeros de Reynolds ha sido llevado a cabo. Varias cantitades tales como, velocidades medias, velocidades instantaneas y presión estática son medidos. Detras del "flameholder" la estela es similar al Vortice de Von Karman. La distribucion de presión alrededor de el "flameholder" muestra

una alta variabilidad correspondiente a la oscilación de las lineas de corrientes. Visualización de las lineas de corriente, contornos de presión y *rms* de velocidad son mostrados en este trabajo.

To my dear family, friends and my little princess, Tany

ACKNOWLEDGMENTS

To Prof. Stefano Leonardi who showed me through his advice which is the way forward of a true investigator.

TABLE OF CONTENTS

LIST OF TABLES

Table page

LIST OF FIGURES

LIST OF ABBREVIATIONS

LBO	Lean Blow Out
CFD	Computational Fluid Dynamics
LDV	Laser Dopple Velocimeter
PIV	Particle Image Velocimetry
LES	Large Eddy Simulation
DNS	Direct Numerical Simulation
RANS	Reynolds Average Navier–Stokes
PDF	Probability Density Function
TKE	Turbulent Kinetic Energy
AIM	Anisotropic Invariant map

LIST OF SYMBOLS

CO	Carbon monoxide
NO_x	Nitrogen oxide
Re	Reynold Number
$\kappa - \varepsilon$	$\kappa - \varepsilon$ model
C_D	Drag coefficient
C_L	Lift coefficient
t	time
η	Kolmogorov microescale
U, V, W	mean velocity components in the (x, y, z) directions respectively
u, v, w	fluctuating velocity components in the (x, y, z) directions respectively
P	mean pressure
p	pressure fluctuation
x, y, z	streamwise, wall-normal and spanwise directions respectively
u_i	fluctuating velocity component in the $x_i \equiv (x, y, z)$ direction
h	channel half-height
$T = h/U$	channel flow non-dimensional time unit $\equiv h/U_c$
U_c	channel centerline velocity
ν	kinematic viscosity
ρ	fluid density
Π	driving force to keep the flow rate constant roughness elements

CHAPTER 1
INTRODUCTION

Climate change (warming of the climate system, increasing global air and ocean temperature, rising global average sea level and reduction of snow and ice) is due mainly to human acitivities that involve primarily the combustion of fossil fuels [1]. Therefore, because of their impact on ecosystem, the pollutions emissions requirement are a stringent condition to considerate in any engineering process, like the combustion in a gas turbine, [2]. The pollution emissions like CO, NO_x and unburnt hydrocarbons (UHC) in these systems are produced by combustion instability, due to very lean fuel–air mixture, during which the flame undergoes rapid oscillations and eventually blows out completely. This process is often called "lean blow out" (LBO). In gas turbine combustion system to achieve low–emissions of pollutions is necessary to stabilize the flame through of used of bluff–body usually called "flameholder", which anchor the flame by creating recirculation zones to provide a continuous ignition source, facilitating the mixing of the injected fuel and incoming air [3]. The flameholder creates a low–velocity zone of sufficient residence time and turbulence levels such that the combustion process becomes self–sustaining [2]. The stability of the flame depends in some way on the residence time of gases in the recirculation zone. (Stability is defined as the range of equivalence ratio over which a flame can be maintained, other conditions being kept constant; the equivalence ratio is the ratio of the fuel present to the amount of fuel required in a stoichiometric mixture). The condition of flame stabilization in a flow field of non–uniform velocity

is that there is a point in the flow field where the flow velocity is equal and opposite to the velocity of the combustion wave.

The flows over objects such as the flameholder are encountered extensively in engineering applications, for example in gas turbines and ramjet engines, high–rise buildings, marine risers, bridges, cooling towers, chimneys, tube banks in heat exchangers and support structures. These objects, which usually create a massive wake of eddies in the stream behind the object are called **bluff bodies**. Bluff body flows are basic flow of great practical importance, occurring in a large number of situation including vehicles moving through air/water such as cars, boats and airplane, or flow of air/water around bodies at rest such as buildings, bridges, off–shore structures or cables. Bluff-bodies used to hold the flame stable are all to be referred as **Flameholder**. The shape of the bluff–body flameholder affects the flow stability characteristics through the influence on the size and shape of the wake region (Lefebvre, *1983* [4]). A bluff–body consists of any immersed object whose downstream shape is blunt enough, which gives the flow turbulent characteristics due to the generation of vortex. The characteristics of the vortex depend on the shape and dimension of the bodies [5]. Since the flame stabilization depends on size of the zone of recirculation behind the bluff–body, different geometries of bluff–body are used. Figure 1–1 shows different geometries of bluff-body such as triangular, rectangular, circular and more complex shapes.

The study of bluff-body flows has been a subject of interest to engineers and scientists for several decades. The abundance of phenomena observed in bluff–body flows is a direct consequence of the fact that these flows are actually composed of three fundamental shear flows, namely the wake, the separated shear layer and the boundary layer, each of which develops instabilities as the Reynold Number (Re) is progressively increased [6]. In the same way, the study of unsteady turbulent wake

behind bluff bodies of different geometries, Figure 1–1, have been and are nowadays extensively subject to many numerical and experimental studies, due to the analytical complexity to resolve the flow equations that governing this phenomenon, and its engineering application, as is the case of bluff–body–stabilized flame in gas turbine. Johansson & Davidson [7] made a numerical and experimental study of an incompressible unsteady two–dimensional flow around and behind a triangular bluff–body flameholder, (Figure 1–1(a)), where the turbulence was modelled using a standard high Reynolds number κ–ε model and the calculated results were compared with experimental data, obtained with laser–Doppler system. The study of different bluff–body geometries is attractive since it allows to investigate the behavior of the flow to various surface conditions. An extensive experimental study of the flow-field downstream of a bluff–body , (Figure 1–1(b)), has been made by Raffoul, *1995* [3].

The flows around the bluff–bodies are called bluff–bodies flows and these can be classified such as 2–dimensional and 3–dimensional bluff–body flow. When one component of velocity of the inflow, upstream the bluff–body is equal zero, then the flow is 2–dimensional, in this case, there are only velocities in two directions, which usually are x–direction and y–direction. In 3–dimensional bluff–body flows, all the components of velocity upstream the bluff–body are different than zero. Simply 2–dimensional and 3–dimensional bluff–body flows have been subject of experimental investigations for a number of years, (Fuji *et al. ,1978* [8]). An experimental investigation of three–dimensional effects in turbulent bluff–body wakes (wake behind a circular cylinder, Figure 1–1(d)), such as parallel shedding, oblique shedding and vortex dislocations, by manipulation of the end conditions, over a large range of Reynolds number, is carried out by Prasad *(1997)*, [6].

One of the basic problems of bluff body flow is to compute the *drag coefficient* C_D, which is a normalized mean value in time of the momentary *drag force* at time

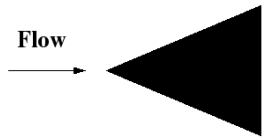

(a) Triangular bluff–body

(b) Bluff–body.

(c) Rectangular bluff–body.

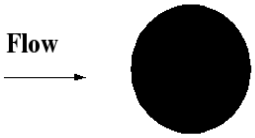

(d) Circular bluff–body.

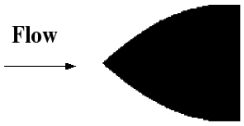

(e) Bluff–body.

(f) Bluff–body.

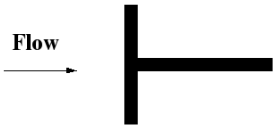

(g) Bluff–body.

(h) Bluff–body.

Figure 1–1: Different geometries of bluff–body

t, and the *lift coefficient* C_L, which is a normalized mean value in time of the *lift force* acting in a direction perpendicular to the flow. The flow around a bluff body at high Reynolds numbers is turbulent in a *wake* attaching to the rear or the body. As the shape of the body gets more streamlined, the wake gets smaller and the drag decreases. The drag has a contribution from the pressure distribution on the body surface, the *pressure drag* or *form drag*, and a contribution from the viscous forces, the *skin friction*. Bluff body flow exhibits basic phenomenon such a *boundary layer flow, separation*, and *transition* from laminar to turbulence flow [9].

Turbulence is a natural phenomenon in fluids that occurs when velocity gradients are high, with velocity fluctuations in the flow domain as a function of space and time [10]. The analysis of turbulence is not easy, particularly in flows with high

Mach numbers and high Reynolds numbers, however its intensive study continues growing in the fields of theoretical, experimental and numerical investigation. The latter being the area of greatest application at present due to the development of modern computational fluid dynamics (CFD) which began with the advent of the digital computer in the early 1950s. The experimental study of turbulent flows is carried out using experimental techniques such as the technique used by laser–Doppler velocimeter (LDV) to measure turbulent velocity fluctuations. LDV has been used for fluid flow measurements since the mid 1960s. In 1964, Yeh & Cummins [11] successfully measured velocity profiles in a liquid (laminar water flow) using laser–Doppler velocimeter, who demonstrated that coherent light sources could be used by observing the Doppler shift in the frequency of light scattered from small particles moving with the fluid, [12]. Since 1964, numerous investigators have used laser–Doppler velocimeter to the measurement of mean–square fluctuating velocities and instantaneous velocities in the unsteady flow of gases and liquids. George & Lumley [12], presented a description of an operational laser–Doppler velocimeter and measurements of spectra in both laminar and turbulent flow. LDV is a non–intrusive instrument used to measure turbulent velocity fields without interferi:wng with the fluid itself, and where conventional techniques (i.e., hot–wire anemometer) are not practical. The laser Doppler method is based on the measurement of the Doppler shift of laser light scattered from small particles carried along with the fluid. Typical applications include turbulent boundary layers, vortices and wakes, such as the recirculation zone behind a bluff–body or a backward–facing step. Raffoul *et al. ,1995* [3], used the laser–Doppler velocimeter to measure the three–component velocity downstream of a bluff–body flameholder. The flow behind triangular flameholders has been investigated experimentally using a laser Doppler velocimeter by Johansson & Davidson [7]. Other recognized as well established non–intrusive technique for fluid velocimetry measurements is the Particle Image Velocimetry (PIV) which

had its genesis several years ago, however its more common usage occurred in the last decade. An important aspect of PIV is its ability to measure the vorticity field and spatial correlations as well as to provide information over a flow field, simultaneously at many points, [13]. Hyun *et al.* [13] described a compressive and quantitative comparison of LDV and PIV measurements of mean velocity, turbulence and other quantities in a relatively complex flow. Other technique used to study the turbulent flow is the smoke flow visualization which is an experimental means of examining the flow pattern around a body or over its surface. The primary advantage of such a method is the ability to provide a description of a flow over a model without complicated data reduction and analysis. Prasad & Willianson [6], used a vertical–wire system to visualize the flow effects in turbulent bluff–body wakes.

Due to the difficulties involved in developing rigorous statistical model of turbulence, the cost of experimental setup, and the rapid development of computer power, it might be argued that the way forward relies on numerical simulation of turbulence [14]. The numerical study of turbulent flows has grown rapidly in the last ten year with the increases of storage resources and computational power. Most of the research currently taking place in the field of computational fluid dynamics (CFD) concerns with the study of turbulence flows. The three major types of numerical turbulence methodologies in CFD are Direct Numercial Simulation (DNS), Large Eddy Simulation (LES), Reynolds averaged Navier–Stokes (RANS) and Probability Density Function (PDF). One important area of application of these numerical techniques is the unsteady turbulent wakes behind a 2–D and 3–D bluff-bodies. At present, the most which can be achieved is to perform numerical simulations at rather modest values of Re and in *extremely* simple configurations. Turbulent flows are composed of eddies which are overlapping in space, with large ones carrying small ones. The scales of eddies ranges from those comparable to the domain of interest down to the Kolmogorov dissipation scale. In DNS a refined mesh is used

so that all these scales, large and small, are resolved in which no turbulence modeling is needed. In DNS, the Navier–Stokes system of equations is solved directly with refined meshes capable of resolving all turbulence length scales including the Kolmogorov microscale, η. DNS is a hard research tool in the study of turbulent flow , and not a brute–forced solution to the Navier–Stokes equations for engineering problems, because significant insight into turbulence physics has been gained from DNS of certain idealized flow that cannot be easily attained in the laboratory due to the complex behavior of turbulence. DNS is the only numerical technique which gives a complete description of a turbulent flow, where the Navier–Stokes equations are resolved. These numerical solution are called direct numerical simulation. DNS is a very useful tool for studying simple flows at low or moderate Reynolds numbers. The foundations of DNS were laid at the National Center for Atmospheric Research. The beginnings were humble: Orszag & Paterson (1972) [15] performed a 32^3 computation of isotropic turbulence at a Reynolds number (based on Taylor microscale) of 35. The next major step was taken by Rogallo (1981) [16], who combined a transformation of the governing equations with an extension of the Orszag-Patterson algorithm to compute homogeneous turbulence subjected to mean strain. The study of Rogallo examined the effects of mean shear, irrotational strain, and rotation on homogeneous turbulence. The pioneering work of Rogallo set the standard of DNS of homogeneous turbulence. Subsequent homogeneous DNS have essentially used his algorithm, [17]. The contribution of direct numerical simulation to turbulence research in the last decade have been impressive. The availability of raw DNS data has spawned a new trend in the field: it small cal it has brought together researchers from diverse disciplines and with diverse viewpoints. The future of DNS in turbulence research appears bright. The greatest strength of DNS is the stringent control it allows over the flow being studied. At the other end is turbulence modeling or RANS methods, where time and small scales of turbulence are modeled

so that mesh refinements needed for DNS are not required. A compromise between DNS and RANS is the large eddy simulation (LES) which has become very popular in recent years. LES is intermediate in complexity between DNS and RANS. Large eddy simulation directly computes the large energy–containing scales in time, while modeling the influence of the small scales. The LES approach is becoming increasingly popular in the community of CFD because of this nature. A numerical study of the flow around a three–dimensional bluff body is carried out using LES by Krajnovic & Davidson [18] which concluded that real–life experiments can be simulated from data obtained in Large Eddy Simulation.

The method used for the present thesis relies on a code, based on a finite different scheme and a Runge Kutta 2nd order accurate coupled with the immersed boundary technique to represent the flameholder. The code can run on a cluster of computers, solving the Navier Stokes Equations on grid with 100,000,000 points. This simulation represents the first Direct Numerical Simulation of a flame holder at an intermediate Reynolds number. With respect to a commercial code, a code is optimized for the particular problem considered and therefore is more efficient. Simulations can be carried out at lower computational cost and at higher Reynolds number. The code has been extensively validated in several papers. Leonardi *et al.* [22] compared the results in a channel with roughness on the lower wall with the experiment by Hanjalic & Launder [20] and Ikeda & Durbin [21]. The mean velocity, total drag and turbulence intensities agree well. In another paper, Leonardi *et al.* [23] verified the grid independence of the results by carrying out a grid refinement, doubling the number of points in each direction. To further validate the code an experiment was designed which could be reproduced in a direct numerical simulation. The mean velocity profiles and rms distributions at three Reynolds numbers overlap closely (Burattini *et al.* [19]).

CHAPTER 2
OBJECTIVES

The aim of the present thesis is to study the flow field behind a triangular bluff–body flameholder. The flameholder produces a recirculation which stabilezes the flow and the combustion. Instabilities in the combustion chamber of a gas turbine are due to the rapid oscillations in the flame. Direct Numerical Simulations (DNS) are performed at intermediate Reynolds numbers using an in house finite difference code. Various quantities such as, mean velocities, recirculation length, turbulent fluctuations, static pressure and root mean squares of velocities are computed. The simulation results are compared with experimental measurements, Large Eddy Simulation (LES), and Reynolds–Averaged Navier–Stokes (RANS).

CHAPTER 3
NUMERICAL PROCEDURE

3.1 Discretisation of the Navier–Stokes Equations

This chapter will attempt to explain the discretization of the Navier-Stokes equations, into a form which can be evaluated numerically. The Navier-Stokes equations have been discretized in an orthogonal coordinate system using the staggered central second-order finite-difference approximation Orlandi [24]. The discretized system is advanced in time using a fractional-step method with viscous terms treated implicitly and convective terms explicitly. The large sparse matrix resulting from the implicit terms is inverted by an approximate factorization technique. At each time step, the momentum equations are advanced with the pressure at the previous step, yielding an intermediate non-solenoidal velocity field. A scalar quantity Φ projects the non-solenoidal field onto a solenoidal one. A hybrid low-storage third-order Runge-Kutta scheme is used to advance the equations in time. This approach allows the solution of flows over complex geometries without the need of computational intensive body-fitted grids.

3.1.1 The physical model

The behavior of fluid flows is described by the Navier-Stokes equation. The equations for viscous incompressible flows are:

$$\frac{\partial u_i}{\partial t} + \frac{\partial u_i u_j}{\partial x_j} = -\frac{\partial p}{\partial x_i} + \frac{1}{Re}\frac{\partial^2 u_i}{\partial x_j \partial x_j} + \Pi\delta_{1i} \ , \tag{3.1}$$

$$\frac{\partial u_j}{\partial x_j} = 0 \ . \tag{3.2}$$

where the physical meaning of Π is that this term, is an external force, which has to be added to the Navier Stokes equation to balance the loss of energy dissipated by friction and pressure drag. This external force maintain the flow rate constant. u_i, the i-component of the velocity vector in the i direction; p the pressure; $Re = (U_c h/\nu)$ is the Reynolds number; h, the channel half-width; U_c, the centerline velocity laminar Poiseuille, i.e. is the velocity of a flow Poiseuille (laminar flow) in the centerline of the channel. and ν, the kinematic viscosity. $u = u^*/U_c$, $x_i = x_i^*/h$, $p = p^*/(\rho U_c^2)$ and $t = t^* U_c/h$ with * denoting dimensional units.

3.1.2 Discretisation

The Navier Stokes equations shown above (equations 3.1 and 3.2) are discretised using a central second-order finite-difference approximation. The scheme is based on a fractional step and factorisation method, accurate to the 2^{nd} order in space and in time.

Stability of the numerical scheme

The governing equations (3.1 and 3.2) are a set of partial differential equations which must be reduced to a set of ordinary differential equations, in time, for each mesh point throughout the domain. The system contains a range of linear and non-linear terms, which must be integrated differently with respect to time. The simplest manner is to treat all terms explicitly. It is not necessary to invert matrices, but limiting conditions imposed for the stability of the solution have to be respected.

The limit due to the explicit treatment of the non–linear term

$$H_i = \frac{\partial u_i u_j}{\partial x_j} \,, \tag{3.3}$$

is known as the CFL condition, named after Courant, Friedrich and Lewis:

$$\left| \frac{u_i \Delta t}{\Delta x_i} \right|_{\max} < 1 \tag{3.4}$$

This means that the distance traveled by a particle has to be less than the mesh width. It should be noted that this evaluation of the CFL condition is valid when only the non-linear terms are considered. Including also the linear terms acts to stabilise the solution, therefore expanding the limit of the condition. In fact in the present thesis all the simulations have been carried out at $CFL = 1.7$.

The second condition, is a convergence criterion arising from the explicit treatment of the linear terms:

$$\frac{\Delta t}{\Delta x^2 Re} < \frac{1}{2n}\,, \tag{3.5}$$

where this inequality is the viscous stability condition, and n is the number of dimensions of the simulation. Of the two conditions equation 3.5 is the most stringent in 3 dimensional simulations as n is at the denominator of equation 3.5. This condition is overcome by the implicit discretisation of the linear terms, which does not require any particular effort, except that to invert tridiagonal matrices.

Discritisation of the linear terms

The scheme used to discretise implicitly the linear terms is the Crank-Nicholson:

$$\frac{du_i^{n+\frac{1}{2}}}{dt} = -R^{n+1/2} + \frac{1}{Re}(A_{1,1} + A_{2,2} + A_{3,3})u_i^{n+\frac{1}{2}} \tag{3.6}$$

where δ is the discrete gradient operator $A_{i,i}$ the linear differential operator relating to the viscous derivative calculated by the central difference scheme, where:

$$A_{1,1} \longrightarrow \frac{\partial^2}{\partial x_1^2} = \frac{{}_1(i+1,j,k) - 2_1(i,j,k) +_1 (i-1,j,k)}{(\Delta x_1)^2} \tag{3.7}$$

$$A_{2,2} \longrightarrow \frac{\partial^2}{\partial x_2^2} = \frac{{}_2(i+1,j,k) - 2_2(i,j,k) +_2 (i-1,j,k)}{(\Delta x_2)^2} \tag{3.8}$$

$$A_{3,3} \longrightarrow \frac{\partial^2}{\partial x_3^2} = \frac{{}_3(i+1,j,k) - 2_3(i,j,k) +_3 (i-1,j,k)}{(\Delta x_3)^2} \tag{3.9}$$

and

$R^{n+1/2} = H_i^{n+1/2} + \frac{\delta P}{\delta x_i}|_{n+\frac{1}{2}}$.

The discrete form of equation 3.10 is:

$$\frac{u^{n+1}-u^n}{\Delta t} = -R^{n+1/2} + \frac{1}{Re}(A_{1,1}+A_{2,2}+A_{3,3})\frac{(u^{n+1}+u^n)}{2} \; . \tag{3.10}$$

Discretisation of the non–linear terms

The discretisation in time of the non linear terms is done by a 3^{rd} order Runge-Kutta. The method was developed by Wray [26]. Let's consider as example the non–linear equation:

$$\frac{du}{dt} = f(u,t) \tag{3.11}$$

which resembles the non–linear terms (H_i) in the Navier–Stokes equations. The requirements for the method are:

1. It is desired that no more than two memory locations are used in the evaluation of $f(u,t)$.
2. The term $u(t)$ is to be evaluated using a Taylor's series expansion.
3. The solution must be repeatable in time i.e.

$$t_l \Rightarrow u_l, f(u_l,t_l) \qquad t_{l+1} \Rightarrow u_{l+1}, f(u_{l+1},t_{l+1}) \; .$$

The satisfaction of point 1 is particularly important when evaluating tridimensional fields whose memory is occupied by data necessary for the scheme. This can impose a serious limit to the calculation. Having information on the initial conditions of u_l and $f(u_l,t_l)$ in equation 3.11, it is possible to create a non-dimensional group of the form $f(u_l,t_l)\Delta t/u_l$. Successive approximations for the value of u can then be gained using the following expression:

$$F\left[f(u_l,t_l)\frac{\Delta t_l}{u_l}\right] u_l \; . \tag{3.12}$$

Although for condition 2, F must be a linear function of the argument, so it can be written as:

$$x' = u_l + a\Delta t_l f(u_l, t_l) \tag{3.13}$$

This occupies the first memory location, the other is occupied by a similar expression:

$$x_A = x_l + A\Delta t_l f(x_l, t_l);\,. \tag{3.14}$$

Computing $f(u_A, t_l + A\Delta t_l)$ we are in the same situation of the initial condition but the solution is advanced in time. Repeating this step l times an accuracy at the l order is achieved. The third order scheme is summarized below:

$$\begin{aligned}
l = 0:\ u_l \quad &| \quad f(u_l, t_l) \\
l = 1:\ u' = u_l + a\Delta t_l f(u_l, t_l) \quad &| \quad u_A = u_l + A\Delta t_l f(u_l, t_l) \\
l = 2:\ u'' = u' + b\Delta t_l f(u_A, t_l + A\Delta t_l) \quad &| \quad u_B = u' + B\Delta t_l f(u_A, t_l + A\Delta t_l) \\
l = 3:\ u_{l+1} = u'' + c\Delta t_l f(u_B, t_l + (a+B)\Delta t_l) \quad &| \quad \text{not used in the 3rd order}
\end{aligned}$$

The '|' character separates the first and second memory positions. Each new line indicates an operation having occurred. When $u_{l=3}$ is gained a new time step can start.

Substituting in $u_{l=3} = u'' + c\Delta t_l f(u_B, t_l + (a+B)\Delta t_l)$ the expression for u'' and u' the third order scheme is finally:

$$u_{l+1} = u_l + a\Delta t f(u_l, t_l) + b\Delta t f(u_A, t_l + A\Delta t) + c\Delta t f(u_B, t_l + (a+B)\Delta t)\ . \tag{3.15}$$

Equation 3.15 is analogous to a Taylor's series expansion for u_{l+1}:

$$u_{l+1} = u_l + \frac{\partial u}{\partial t}\Delta t + \frac{\partial^2 u}{\partial t^2}\Delta t^2/2 + \frac{\partial^3 u}{\partial t^3}\Delta t^3/6\ . \tag{3.16}$$

Expressing the terms $f(u_A, t_l + A\Delta t)$ and $f(u_A, t_l + A\Delta t)$ in Taylor, second and third temporal derivative are obtained. Equating coefficients the following system

is obtained:

$$\begin{aligned} a+b+c &= 1 \\ (a+B)c+Ab &= \tfrac{1}{2} \\ (a+B)^2c+A^2b &= \tfrac{1}{3} \\ ABc &= \tfrac{1}{6} \end{aligned} \tag{3.17}$$

The array of equations contains a total of four equations and five unknown variables, implying that an infinite number of solutions exist. This is solved by the arbitrary assignation of b to zero. The solution is:

$$a=\frac{1}{4} \qquad b=0 \qquad A=\frac{8}{15} \qquad B=\frac{5}{12} \qquad c=\frac{3}{4}\,. \tag{3.18}$$

The procedure used previously is applied to the non–linear term of the Navier–Stokes equation ($dU/dt = H_i$):

$$\begin{aligned} l=1: \; u_l &= u_{l-1}+\gamma_1\Delta t H_{l-1} \\ l=2: \; u_l &= u_{l-1}+\gamma_2\Delta t H_{l-1}+\rho_2\Delta t H_{l-2} \\ l=3: \; u_l &= u_{l-1}+\gamma_3\Delta t H_{l-1}+\rho_3\Delta t H_{l-2}\,, \end{aligned} \tag{3.19}$$

where "l=1,2,3" are the three Runge Kutta steps. In the first equation of the array (3.19) the term ρ_1 does not occur. For the first step the only term available is $f(u_l, t_l)$, since there is no information from any previous step.

It is possible to substitute this condition (3.23) into the system of equations (3.19) to get the result shown in equation 3.20.

$$u_{l+1} = u_l + \Delta t[(\gamma_1+\rho_2)N_l + (\gamma_2+\rho_3)N' + \gamma_3 N'']\,. \tag{3.20}$$

The coefficients of each term can then be equated with those from equation 3.15. This produces a system of five equations with five unknowns (3.21). The solution for the variables is shown in array 3.22.

$$\begin{aligned} a &= \gamma_1 + \rho_2 \\ b &= \gamma_2 + \rho_3 \\ c &= \gamma_3 \\ A &= \gamma_1 \\ B &= \gamma_2 \end{aligned} \tag{3.21}$$

$$\begin{array}{lll} \gamma_1 = \frac{8}{15} & \gamma_2 = \frac{5}{12} & \gamma_3 = \frac{3}{4} \\ \rho_1 = 0 & \rho_2 = -\frac{17}{60} & \rho_3 = -\frac{5}{12} \end{array}$$

The complete scheme is obtained. Merging linear and non linear terms:

$$\frac{u_i^{l+1} - u_i^l}{\Delta t} + \gamma H_i^l + \rho H_i^{l-1} = -\left.\frac{\delta P}{\delta x_i}\right|_{l+\frac{1}{2}} + \alpha_i \frac{1}{Re}(A_{1,1} + A_{2,2} + A_{3,3}) \left(\frac{u_i^{l+1} + u_i^l}{2}\right) \ . \tag{3.22}$$

where $l+1$ and l are the new and old Runge Kutta steps respectively with $l = 0$ coinciding with n and $l = 3$ with $n+1$. In order for all the terms to move forward in time at the same rate, i.e. same Δt, it is necessary to impose the condition:

$$\alpha_i = \rho_i + \gamma_i \ . \tag{3.23}$$

It must be remembered that this scheme is second order accurate with respect to the linear terms and third order with respect to the non-linear terms. This difference being due to the nature of the discretisation in space of each type of term.

Equation 3.22 is discretised about the point $l + \frac{1}{2}$ for a solution at $t = l + 1$. This, however, is not physically correct for the pressure terms because it is unknown at $t = l + \frac{1}{2}$ and P at $t = l$ is used. As a consequence an attempt solution $\hat{u}$ is

found which has to be corrected to get a solenoidal velocity field. By introducing $\Delta u = \hat{u} - u_i^l$ equation 3.22 becomes 3.24:

$$\frac{\Delta u}{\Delta t} - \alpha \frac{1}{Re}(A_{i,i})\frac{\Delta u}{2} = \gamma H_i^l + \rho H_i^{l-1} - \frac{\delta P^l}{\delta x_i} + \alpha \frac{1}{Re}(A_{i,i})u_i^l \tag{3.24}$$

In order to resolve equation 3.24 we must invert a sparse matrix with seven sets of diagonal elements. The computational cost of a direct inversion is extremely high, so instead a three step factorisation is employed as suggested by Kim & Moin [43] in 3.25:

$$\begin{aligned} (I + \Delta t \cdot A_{1,1})\Delta u^{**} &= RHS \\ (I + \Delta t \cdot A_{2,2})\Delta u^{*} &= \Delta u^{**} \\ (I + \Delta t \cdot A_{3,3})\Delta u &= \Delta u^{*} \ . \end{aligned} \tag{3.25}$$

This scheme, second order accurate in two dimensions, allows calculation of the value $\hat{u}$. To find the divergence free field at the new time step u^{l+1} a scalar quantity Φ is introduced:

$$u_i^{i+1} = \hat{u}_i - \Delta t \frac{\delta \Phi}{\delta x_i} \tag{3.26}$$

$$L_{jj}\Phi = \mathrm{div}\hat{u} \tag{3.27}$$

Finally the pressure is calculated from

$$p^{n+1} = p^n + \Phi - \beta L_{jj}\Phi \ . \tag{3.28}$$

where $\beta = \frac{\Delta t \alpha}{2Re}$ and L_{jj} is the Laplacian operator, jj was adopted as subscript, could take another. To resume, the integration in time from iteration n to $n+1$ is composed of 3 Runge Kutta steps ($l = 1, 3$). For each step (l) the pressure at the previous time step is used, and hence an intermediate solution $\hat{u}$ is found. The inversion of the 7 diagonal matrix due to the implicit linear terms is done trough

a factorization. This solution $\hat{u}$ is projected into a solenoidal field using the scalar quantity Φ.

3.1.3 Coordinate System

A *staggered* grid is used to keep the differential operators as compact as possible, this is shown in figure 3–1. The pressure is defined at the center of each cell and the velocities at the centre of the faces. The vorticity is naturally defined at the edges and from this position can be calculated at the most useful location (usually the centre) by a linear interpolation.

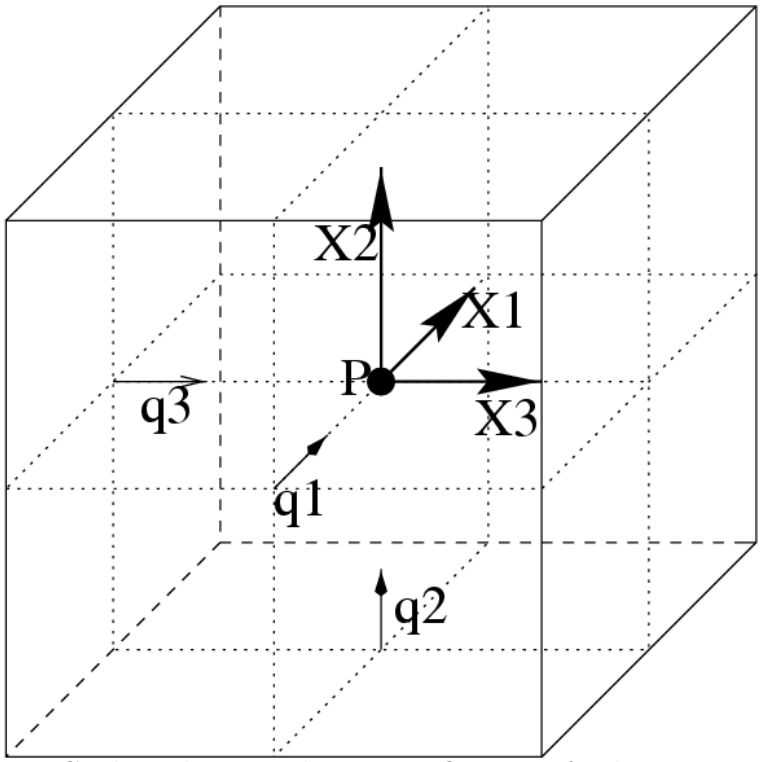

Figure 3–1: Grid used in simulation. Definition of velocities is included.

3.1.4 Immersed boundary method

Complex geometry flows requiring body–fitted curvilinear or unstructured meshes are still challenging problems for today computers for the amount of memory requested and the low efficiency compared to codes in orthogonal grids. Moreover a

statistical analysis is reasonable if the number of samples is large. In the case of turbulent flows over flat wall, averages and moments are computed in time and also in the homogeneity directions, thus reducing the number of velocity fields needed. In a general 3 dimensional rough wall there are no homogeneity directions and then a larger number of fields has to be stored to have the same convergence of the statistics. Hence to have more fields, simulations have to be carry out for a longer time. Finally, as the roughness of interest in engineering are much smaller then boundary layer thickness or channel half–width, points have to be clustered near the roughness elements. Then, in this region, Δx_i is little and a decrease in Δt is mandatory to maintain CFL in the stability limit. All this factors combined with the low efficiency of body–fitted codes made impossible to study roughness numerically.

A new opportunity is given by immersed boundary methods, or body force methods which allows to handle roughness in orthogonal grids thus retaining the accuracy and high efficiency of the simulations performed on fixed regular grids. The computational grid is orthogonal and boundary body forces or masking methods allow the imposition of the boundary conditions on a given surface not coinciding with the computational grid.

Several methods have been developed in the past. Peskin [27]–[28] reports at the beginning of the seventies simulations of the blood flow in the mitral valve and in the heart assuming a very low Reynolds number and two–dimensional flow. Three-dimensional heart flows were considered successively by McQueen & Peskin [29]–[30] that included also the contractile and elastic nature of the boundary. In the above papers, the motion of the boundary was determined by the flow and only the forces occurring between boundary elements were known. Within this framework, solid boundaries were modeled by elements linked by very rigid springs even if the computation of the force system remained as complex as in the case of elastic boundaries. In contrast if the boundary configuration is known the computation of

the body force distribution becomes much simpler since for every boundary element only local information is needed instead of the complete force distribution over the boundary. Accordingly, Briscolini & Santangelo [31] used an immersed boundary approach (referred to as mask method) to compute the unsteady two–dimensional flow around circular and square cylinders at Reynolds numbers up to 1000. Goldstein, Handler & Sirovich [32] considered the two-dimensional startup flow around a circular cylinder and three–dimensional plane– and ribbed–turbulent channel flow. In the last two papers the immersed boundary technique was combined with spectral methods and spurious oscillations at the boundary appeared if the forcing was not spread over several $(3-4)$ grid points across the boundary. Saiki & Biringen [33] used the forcing of [32] to compute the flow around steady and rotating circular cylinders using fourth order central finite–difference approximations. Indeed the use of finite–differences avoided the appearance of spurious flow oscillations at the boundary even if also in that case the forcing was spread across the boundary using a procedure that the authors refer to as 'first–order accurate similar to the delta–function of Peskin [27]. The main drawback of the forcing introduced in [32] is that it contains two free constants that need to be tuned according to the frequencies of the flow and the higher the magnitude of the constants the stiffer the equations become. This implies that for strongly unsteady flows the time step size must be reduced to small values thus making the application of the method expensive. Even with this drawback, however, the method is always more convenient than the classic body–fitted mesh approach and it has been recently used for the simulation of three–dimensional flows by Goldstein, Handler & Sirovich [34], Goldstein & Tual [35], Saiki & Biringen [36] and Arthurs *et al.* [37].

Recently Mohd–Yusof [38] derived an alternative formulation of the forcing that does not affect the stability of the discrete–time equations. In addition, in this case there are no free constants, making the derivation of the body force distribution is

flow independent. In [38] the new forcing was combined with B–splines to compute the laminar flow over a three–dimensional ribbed channel, showing substantial improvements with respect to the previous formulations. This discrete–time forcing scheme was originally developed in a spectral context and has also been successfully applied to flows around cylinders and spheres, at moderate Re.

The method employed for the present thesis is similar to the one described by Fadlun *et al.* ([25]). The Navier–Stokes equations are solved in the region of the flow as in equation (3.24) while inside the body a non–slip condition is imposed:

$$\Delta u_{i,j,k} = V_b(\mathbf{x}, t + \alpha_i \Delta t) - V_b(\mathbf{x}, t) = 0 \ . \tag{3.29}$$

where: $\Delta u_{i,j,k}$, represents the velocity difference in the grid point occupied by the body. Equation 3.29 imposes that at each iteration the velocityin the grid points occupied by the body are equal to the body velocity (V_b). In principle there are no restrictions for the velocity distribution or for the shape and motion of the body; therefore a wide variety of boundary conditions can be imposed. In case of moving boundaries traditional codes require regeneration or deformation of the grid which has an high computational cost; with the immersed boundary method, the grid is the same for the entire simulation thus reducing the computational cost. As the flameholder studied in the present thesis does not move but is fixed at the center of the channel, equation 3.29 takes the easier form:

$$\Delta u_{i,j,k} = 0 \ . \tag{3.30}$$

If only equation 3.30 is applied the geometry is described in a stepwise way (---) and the accuracy of the method is low. According to Fadlun *et al.* [25], the velocities at the point closest to the boundary (fig.3–2 $\times$) are evaluated by a linear interpolation,

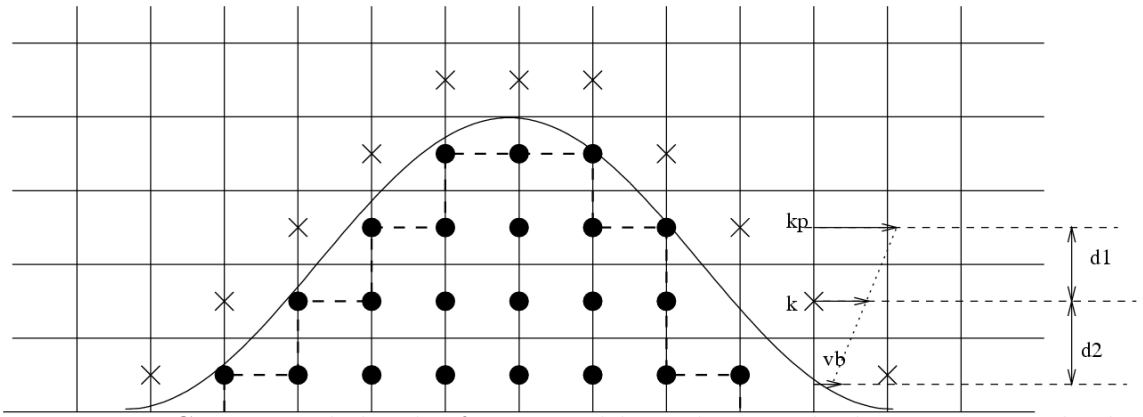

Figure 3–2: Geometrical sketch of immersed boundary method. ∘ points inside the roughness element; × points nearest to the boundary of the roughness element.

and a second order accuracy is achieved.

$$\Delta u_{i,j,k} = u_{i,j,k+1}(t + \alpha_i \Delta t)\frac{\Delta_1}{\Delta_1 + \Delta_2} - u_{i,j,k}(t). \tag{3.31}$$

This assumption respects the physical behavior near the solid boundary of the velocity field which even in turbulent flows is almost linear. This method, hence, requires a fine grid as the basis of DNS.

3.1.5 Flow rate constant

In the present simulations a constant flow rate is imposed. As energy is dissipated because of the friction and pressure drag, an external force is computed to maintain the flow rate constant. Integrating the Navier Stokes equation in the x direction in the whole domain of the computational box is obtained:

$$\int_S \frac{\partial u_1}{\partial t} + \frac{\partial u_1 u_j}{\partial x_j} \cdot dx_1 dx_2 dx_3 = \int_S -\frac{\partial P}{\partial x_1} + \frac{1}{Re}\frac{\partial^2 u_1}{\partial x_j^2} \cdot dx_1 dx_2 dx_2 \ . \tag{3.32}$$

Where S is the flow domain and u_1, is velocity in streamwise direction. For the periodicity in x and z, and being $u_i = 0$ on the walls of the channel it is obtained:

$$\frac{\partial Q}{\partial t} = \frac{1}{Re}\int_S RHS \cdot dx_1 dx_2 dx_3 + \Pi \cdot S \ , \tag{3.33}$$

where RHS is the right hand side of equation 3.32, and Q is the total mass. As a constant flow rate is requested $\frac{\partial Q}{\partial t} = 0$ is imposed and hence eq.3.33 is reduced to:

$$\Pi = -\frac{1}{S}\frac{1}{Re}\int_S RHS \cdot dx_1 dx_2 dx_3 \ , \tag{3.34}$$

where Π is the force which has to be added at the right hand side of the Navier Stokes equation to keep the mass constant. This force is computed at each time step.

CHAPTER 4
2D FLOW OVER A TRIANGULAR FLAMEHOLDER

4.1 Geometrical Configuration

A direct numerical simulation of the two dimensional flow over the triangular flameholder has been performed. The geometrical setup consists of a 300mm x 50mm channel flow (wx2h) with a transverse equilateral triangular rod of base 25mm (b), called **bluff body** placed at the center of channel. A schematic diagram of the bluff body flameholder is depicted in Figure 4–1.

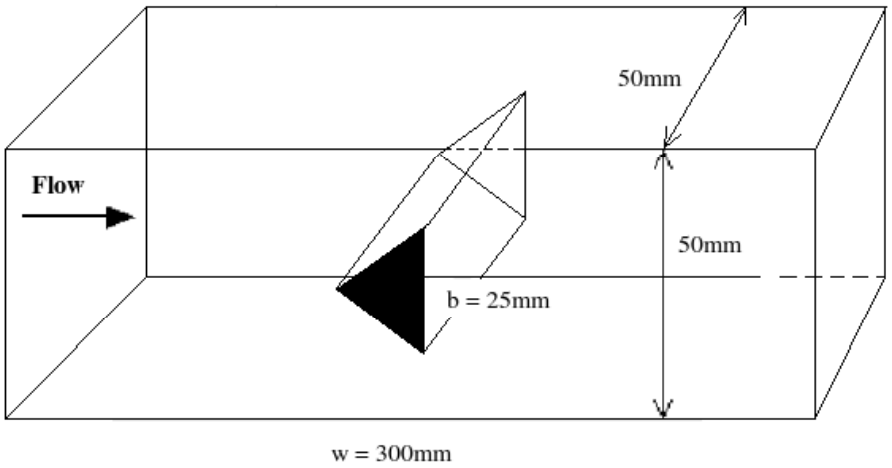

Figure 4–1: Shematic of the bluff body flameholder.

A first task of the thesis was to perform a 2–D simulation of the flow past the 2–D flameholder. The flow configuration (A 2D channel flow with triangular rod at the center of the channel) is shown in Figure A.3, (h = is the half-width of the channel). The upper and lower walls are smooth, and there is a no-slip condition at these walls. Periodic boundary conditions apply in the streamwise (x) direction.

The non dimensional computational domain is 12x2 in the x and y direction (y is the direction normal to the smooth wall), respectively with $h = 25mm$ the reference length to scale distance. The origin in x and y are at the inflow and lower wall, (Figure A.3).

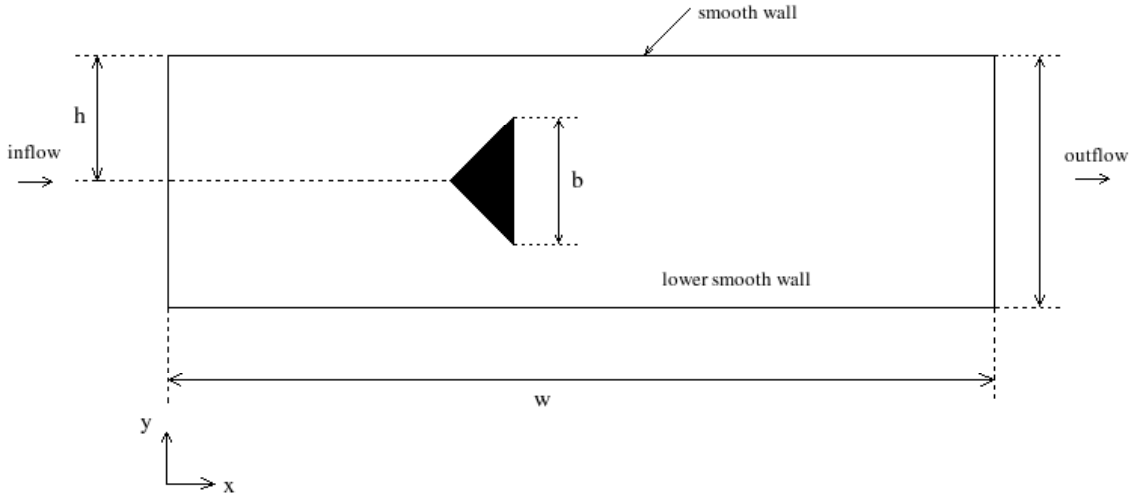

Figure 4–2: Computational flow configuration.

The adimensionalized 2D channel flow is shown in Figure 4–3.

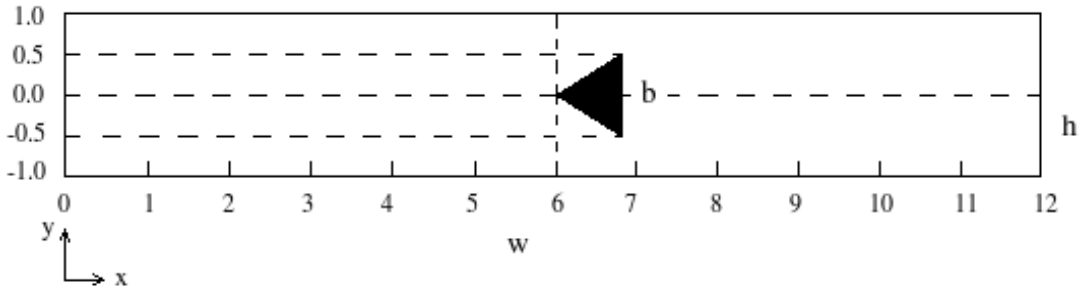

Figure 4–3: Adimensional turbulent channel flow.

The computational grid is in 401, 257 the x, y respectively. The two-dimensional mesh corresponding to this grid, 257x401, is shown in Figure 4–4. This two-dimensional mesh is used to simulates a turbulent flow over a bluff-body flameholder. One of the vertices of the bluff-body is located in point (129,201) in the grid. This point corresponds to the central point of the turbulent channel flow, Figure A.3.

The body side length is h, mounted at the center of a rectangular channel of length $12h$, height $2h$, at a distance of 6h from the inlet. The bluff–body is subject

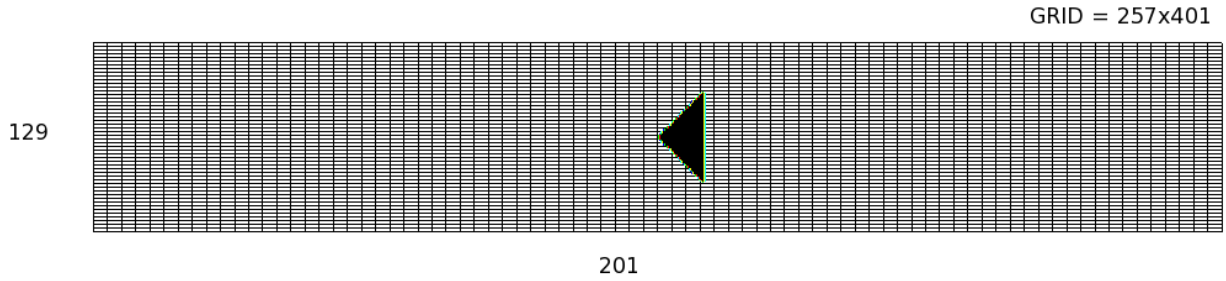

Figure 4–4: Structured mesh 257x401 vertices.

to the Navier–Stokes equations with kinematic viscosity ν and inlet bulk velocity corresponding to a Reynolds number of 100, using the dimension of the base of the bluff–body as characteristic length

4.2 Boundary Condition

In DNS, specifying boundary conditions at open boundaries is a difficult issue, the major difficulty is posed by the inflow and outflow boundary condition where if complex flows are to be computed, turbulent inflow and outflow boundary condition are required. In the case of statistically homogeneous direction such as the streamwise direction in a two–dimensional channel flow, periodic conditions are imposed.

Many flows that have been studied by DNS have one or more directions of homogeneity, that allow the application of periodic boundary conditions. Periodic boundary conditions imply that the computational domain repeats itself and infinite number of times. This conditions are convenient, since they eliminate the need to specify inflow and outflow conditions, easy to implement and efficient, allowing the use of small computational domain.

The use of periodic boundary conditions is similar to studying the time development, rather than the spatial development, of a flow; if one looks at the spatial evolution of a perturbation in plane channel, Figure 4–5, for instance, the use of periodic boundary conditions is equivalent to studying the flow in a convecting frame of reference. Each flow realization(*i.e.*, each time–step) is equivalent to one location in the spatially developing framework. When periodic boundary condition are

used, the computational domain must be at least as long as the wavelength of the longest structure present in the flow. If such wavelength is not known a priory, the two–point correlation must be examined to determine whether the domain length is sufficient.

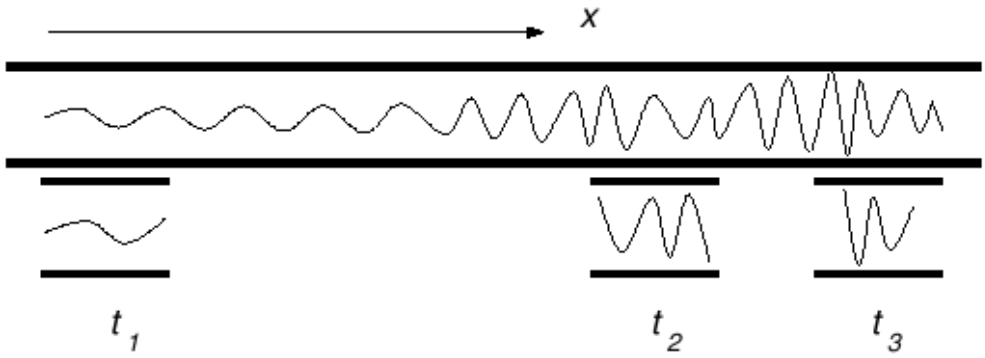

Figure 4–5: Evolution of perturbation in a channel: spatial *vs.* temporal development.

The periodic boundary condition approach works very well for a limited class of flows, however the difficulty appears for complex flows. Spalart (1998) devised an ingenious coordinate transformation to overcome this limitation in DNS to study an evoluving turbulent boundary layer. The transformation allowed periodic boundary conditions to be used in the streamwise direction while generating a statistically stationary turbulent flow whose statistics corresponded to a single experimental streamwise direction [17].

When the flows are not homogeneous in space, the specifications of inflow and outflow conditions is required in many cases. Several studies have focused on the outflow conditions; at present it appears that the use of a buffer domain in which the equations are parabolized, of convective boundary conditions, or a combination of the two techniques, can give adequate results in most flows of interest. The specification of the inflow conditions can, however, be more problematic, since the flow variables on the entire inflow plane must be specified as a function of time. To

study transitional flows, perturbations can be superimposed to a laminar mean flow. This approach has been used successful in boundary layers and mixing layers.

Since our work is devoted to understand the flow behavior near the flameholder for sake of simplicity, we used periodic boundary conditions in the streamwise direction. This is similar to an infinite number of flameholders separated by $12h$. The length of the computational domain is enough to have the flow uncorrelated. Other boundary condition very important, is the wall boundary condition. In this work no–slip boundary condition is used at both the upper and lower walls. Differentiation of the velocity profile to determine the viscous stress, however, is accurate only if the wall–layer is well–resolved.

4.3 Streamlines and Pressure contours

In the present study, the bluff–body flameholder generates the disturbance to the flow. The magnitude of this disturbance is different according to the value of Reynolds number. Downstream the bluff–body the flow passes through a complicated sequence of spatial changes, they induce an unstable behaviour and disordered flow. The Figure 4–6, shows streamlines superimposed to contours of pressure for different Reynolds numbers.

For $Re = 20$ (Figure 4–6(a)), the separation region is rather symmetric. The disturbance downstream the bluff–body after about $2h$ is very similar to its original state before being affected by the bluff–body. In fact the flow is parallel with negligible vertical velocity disturbance. This prove that for low Reynolds number the flow is stable. For higher Reynolds number the instability is clearly appreciated (Figure 4–6(b) and 4–6(c). Counter rotating vortices deattach from the flame holder and are convected downstream. The viscosity is too low and vortices are not dissipated but re–enter in the domain because of the periodic boundary conditions. The streamlines are undulated and the stagnation point move up and down the

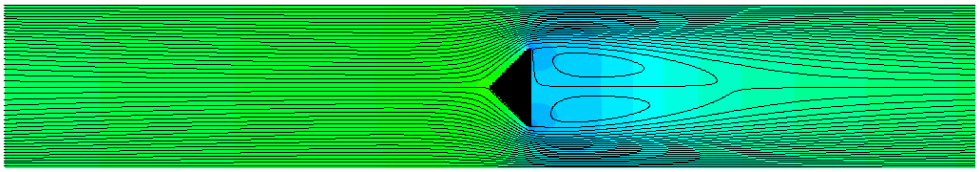

(a) For Re = 20

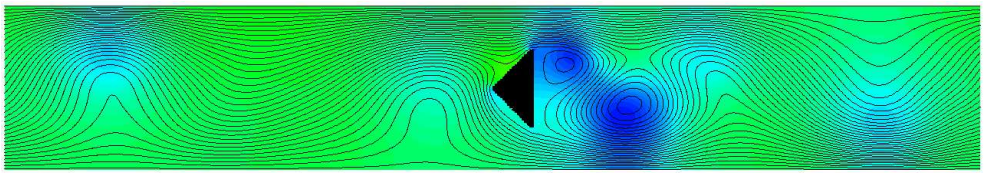

(b) For Re = 100.

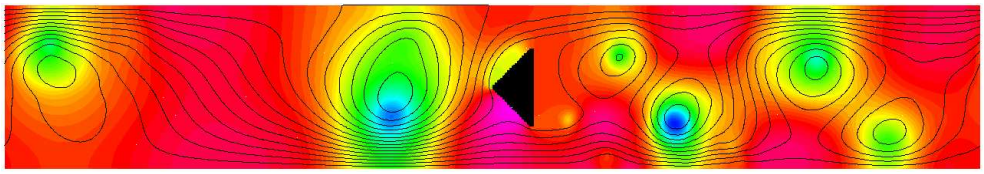

(c) For Re = 1000.

Figure 4–6: Streamlines and pressure at different Re

leading edge of the bluff–body. This is an indication that the flow is unstable. The perturbation given by the flameholder is not dissipated before the next body.

Stability is a concept that has been discussed many time, since Prandtl (1921) who predicted physically that all types of laminar profile becomes unstable at finite Reynolds numbers. The laminar flows have poor resistance to high Reynolds numbers being always turbulent at higher Reynolds numbers, i.e., disorderly, randomly unsteady, apparently impossible to analyze exactly. For any given laminar flow, there is a finite value of its Reynolds numbers which threatens its existence, this value is called critical Reynolds number. Thus laminar flow is found to be unstable, and its critical Reynolds numbers are of such a magnitude that flows of low–viscosity fluid (water, ammonia, gases, ...) are normally turbulent, not laminar. Meanwhile, laminar flow should not be disregarded, because many practical situations arise which are indeed laminar, such as low–speed flows, small–scale bodies, very viscous fluids, or leading–edge problems. In the study of the stability of laminar flow there are two key words to consider, *stability* and *transition*. A physical state is stable if withstand a disturbance and still return to its original state, if not,

that particular state is unstable. The figure, Figure 4–7, shows a ball at rest under various conditions.

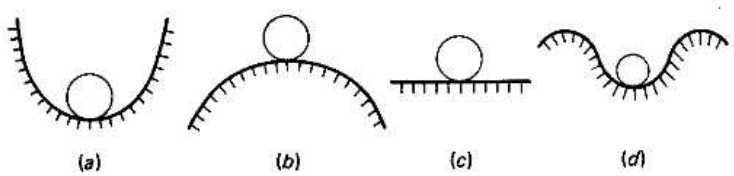

Figure 4–7: Relative stability of a ball at rest: (a) stable, (b) unstable; (c) neutral stability; (d) stable for small disturbances but unstable for large ones

In Figure 4–7 a, its position is unconditionally stable, because it would return to its initial position even if disturbed by a large displacement. On the other hand, Figure 4–7 b, shows a unstable state, since any slight disturbance would topple the ball, never to return. Figure 4–7 c shows a neutral stability since the ball will rest anywhere it is displaced. The last case is shown in the Figure 4–7 d, which illustrate the more complicated case, where the ball is stable for small disturbance displacements but it will diverge if disturbance far enough to drop over the edge.

The stability of a laminar flow is directly related to Reynolds number when it increases, the flow changes to another state, which is generally called turbulence. The transition is defined as the change, over space and time and a certain Reynolds number range, of a laminar flow into turbulent flow. Although the concepts of instability and transition were well established from the work of Reynolds (1883) this is still not well understood and reflected our limited knowledge of this mechanics. Historically, opinions about transition have shifted from one concept to another.

The initial condition of the simulations is a parallel laminar flow. The bluff–body induces a separation to the flow. The separated flow rolls into vortices which are convected downstream and constitute the wake of the body (see Figure 4–8).

Since periodic boundary condition apply in the streamwise direction, all the flow existing at the outflow re–enters in the inflow. Therefore, the vortices generated by the bluff–body in the wake, re–enter in the domain downstream of the bluff–body.

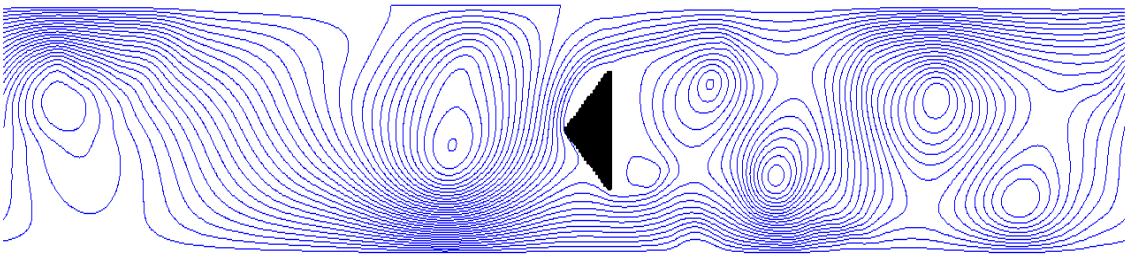

Figure 4–8: Streamlines at t=100 for $Re = 1000$

This explain the wavyness upstream of the wedge. This flow can be considered unstable because the flow never returns to its initial condition (parallel laminar). Instead at $Re = 20$, the vortices generated by the flameholder are rapidly dissipated and it can be considered stable.

The periodicity effect can be observed in Figure 4–9, where of inlet and outlet flow have the same behavior.

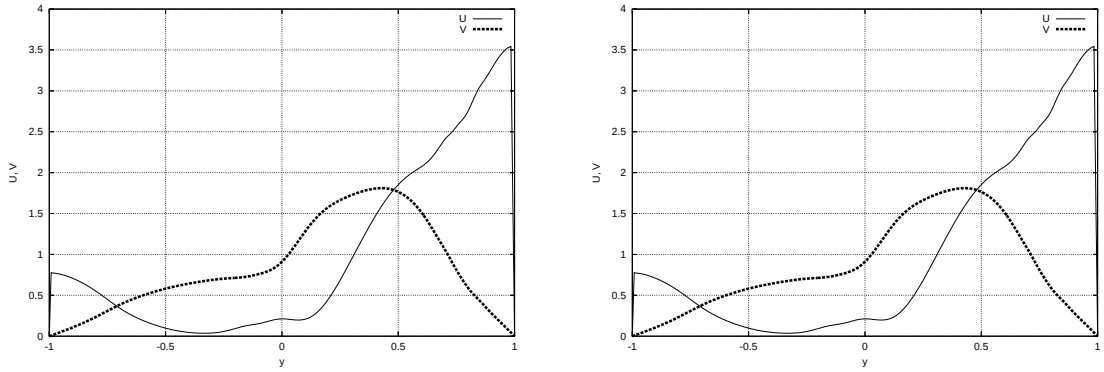

(a) Outflow instantaneous velocity profile (b) Inflow instantaneous velocity profile

Figure 4–9: Periodicity in the channel flow.

The instantaneous velocity and pressure profile along the centre-line ($y = 0$) of the grid 257x401 are shown in the Figures 4–10 and 4–11. The Figure 4–10 shows that the velocity profile before and after of the bluff-body flameholder have a non-uniform behavior and there is a region along the centre-line, in which the velocity is zero. This region corresponds to the grid points of the bluff-body, in the immersed boundary. In the center of the channel flow,$(y = 0, x = 6)$, the instantaneous velocities $u(y, x)$ and $v(y, x)$, are zeros respectively.

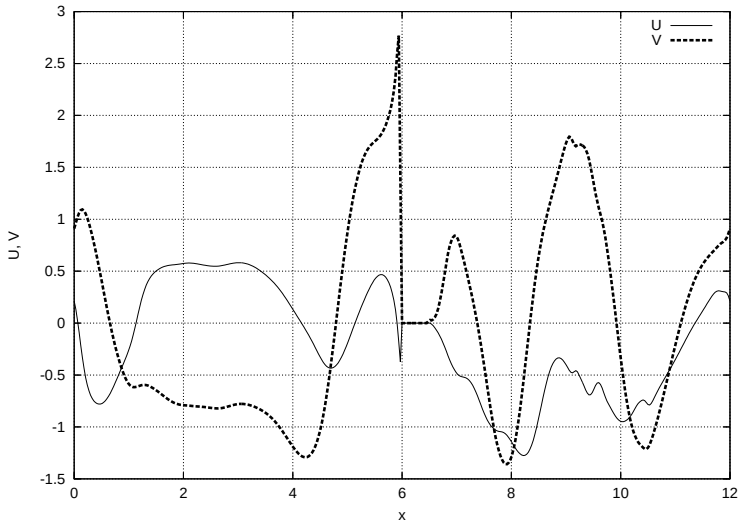

Figure 4–10: Velocity profiles at the centre-line, $y = 0$

Other important aspect to mentioned, is that the velocity before and near of the bluff–body changes of an upper velocity to a lower velocity, until becoming zero in w = 6, Figure 4–11.

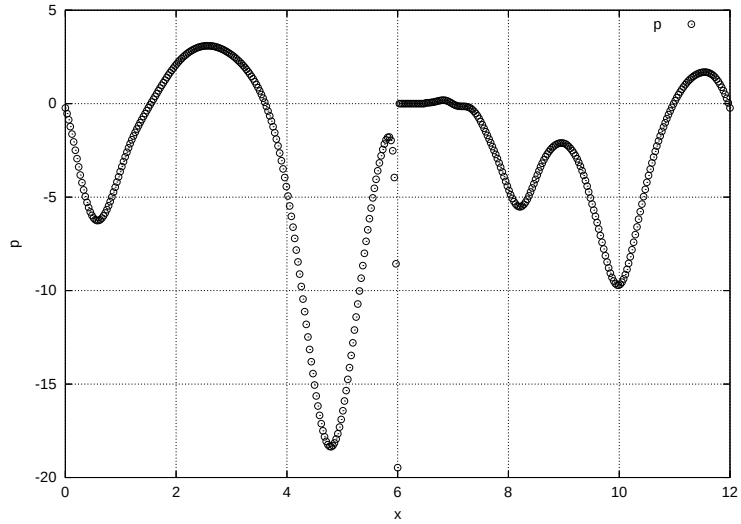

Figure 4–11: Pressure profile at the centre-line, $y = 0$.

The Figure 4–12 shows the velocity and pressure profile, immediately before the bluff–body ($x = 6$). The Figure 4–12(a) shows that there is a point of maximum pressure between $y = 0$ and $y = 0.5$, below the bluff–body. This point is near of the stagnation point, which will be localized in the next section.

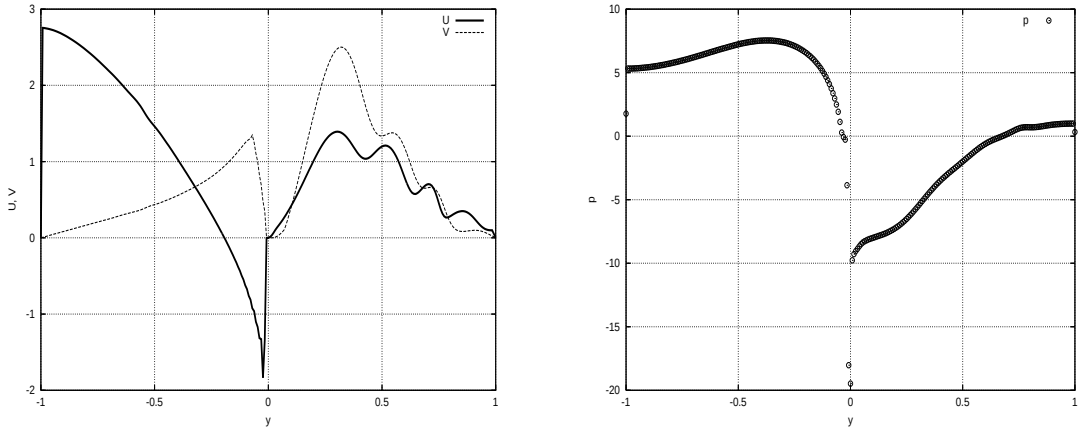

(a) Instantaneous velocity for x=6 (b) Instantaneous pressure for x=6

Figure 4–12: Comparison of the velocity profile and pressure.

The behavior of the inflow, along the channel flow is affected by the bluff–blody flameholder, which gives to the fluid a disturbance. The Figure 4–10 shows this effect. As the flow advances throughout the channel, the velocity is receiving this behavior, until this becomes very disordered after the bluff-body. This can be observed in Figure 4–13, which shows the velocity profiles 3h upstream of the body ($x = 3$), near the body ($x = 6$), immediately after the body ($x = 7$), and 3h downstream of the body ($x = 9$).

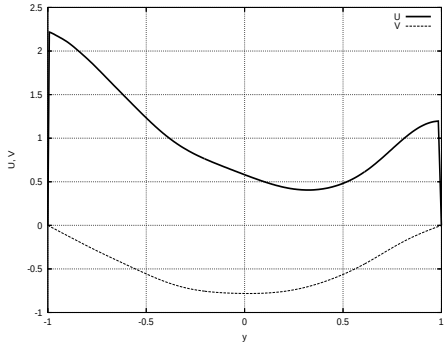

(a) Velocity profile for $x = 3$

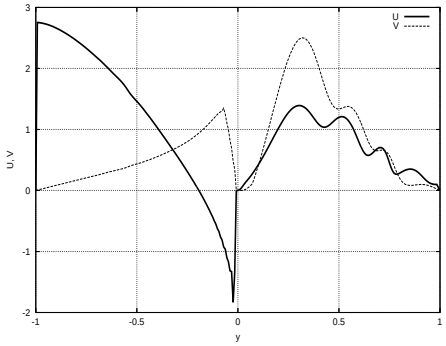

(b) Velocity profile for $x = 6$.

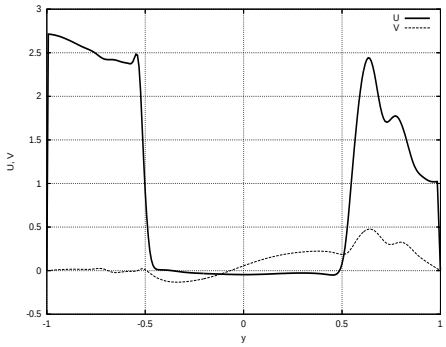

(c) Velocity profile for $x = 7$

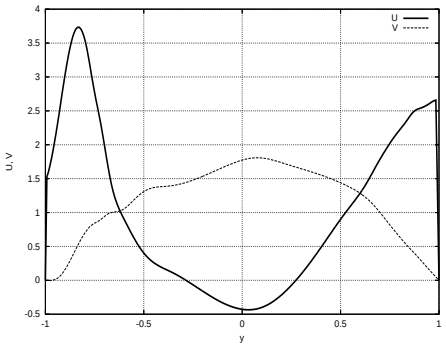

(d) Velocity profile for $x = 9$.

Figure 4–13: Velocity profiles for four section along the channel

The Figure 4–13 shows that the no-slip condition in the lower and upper wall, along the turbulent channel is satisfied.

The determination of instantaneous velocities using DNS is one of our important objectives presented in this study. Figure 4–14 shows the behavior of the instantaneous velocities in streamwise and normal direction for $Re = 1000$. In both graphs there are recirculation zones behind the bluff–body. Figures 4–14(a) and 4–14(b), represent velocity contours, where the red contours represent negative velocities and the blue contours represent positive velocities along the channel flow.

Figure 4–14(a) shows that there is separation in the boundary layer on both, upper and lower side of the bluff–body. *Separation* in a boundary layer occurs where the tangential flow velocity changes sing and *recirculation* occurs. Separation is caused by a positive pressure gradient in the streamwise direction, resulting in a force opposing the flow with a retarding effect. If the adverse pressure force is strong enough over sufficiently long time, the tangential velocity may change sing

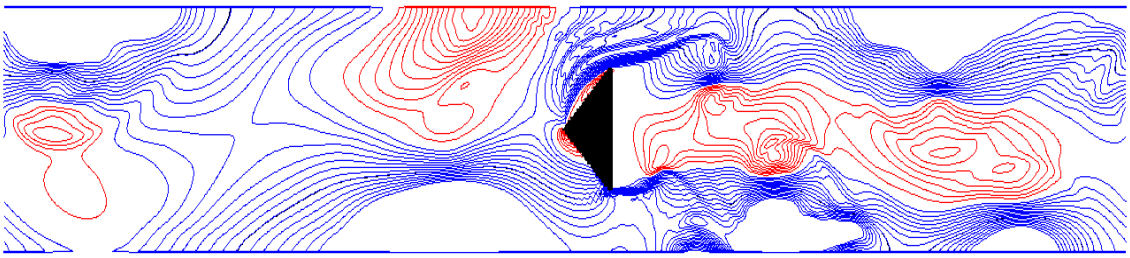

(a) Contours of streamwise direction

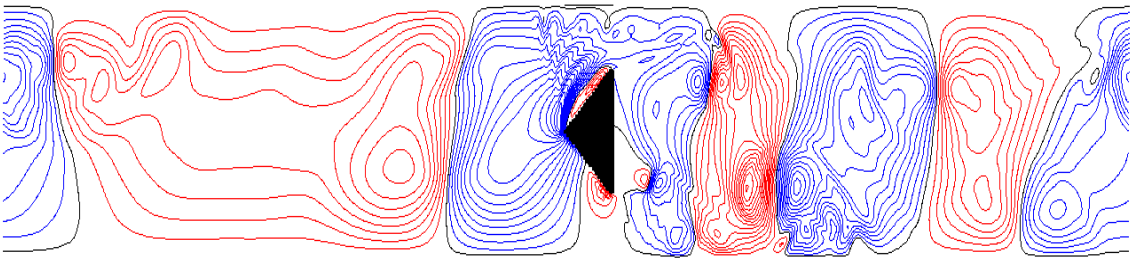

(b) Contours of normal velocity

Figure 4–14: Instantaneous velocity contours, $u(x, y)$ and $v(x, y)$

and separation will occur, [9]. The Figure 4–15, shows contours of instantaneous pressure and velocity very near the bluff–body at $Re = 1000$

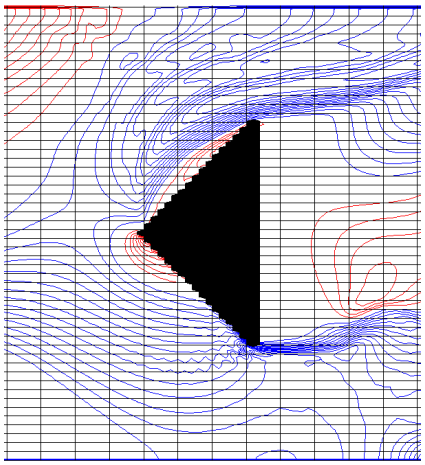

(a) Contour of velocity

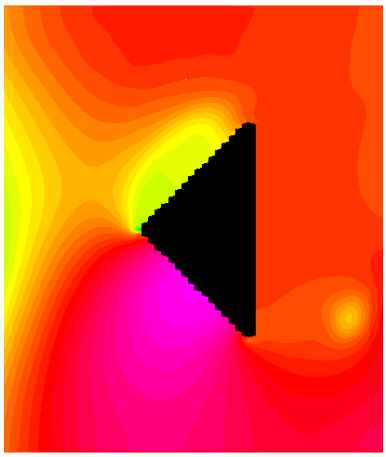

(b) Contour of pressure

Figure 4–15: Velocity and pressure contours at $Re = 1000$

The maximum pressure is represented by the color violet and the minimum pressure by the color blue.

The stagnation point is obtained for about $y = -0.3$; in fact from the streamlines we can see that they are downward. On the upper side the pressure is very low (negative value is relative to the mean pressure and represent a fluctuation).

The high pressure gradient from the stagnation point to the upper side of the wedge leads to an increase of velocity in the upper part of channel.

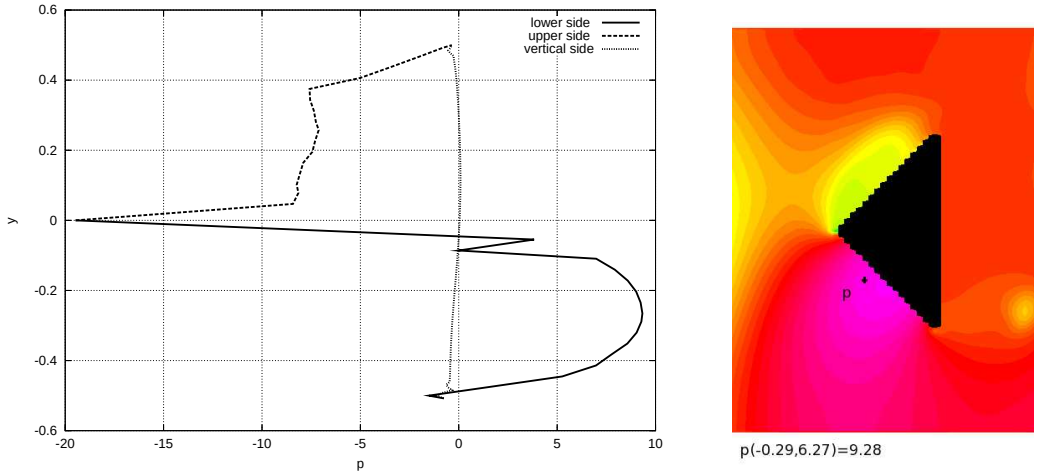

(a) Pressure profile near of bluff–body (b) Stagnation point

Figure 4–16: Pressure behavior

The Figure 4–16, shows the pressure profile in each side immediately next the body. The maximum pressure corresponds to the **stagnation point**. The stagnation point is at $y = -0.29(n2 = 92)$ and $z = 6.27(n3 = 210)$, and pressure is $p = 9.28$ and the coordinates are: $y = -0.29(n2 = 92)$ and $z = 6.27(n3 = 210)$.

4.3.1 Reynolds number dependence

Figure 4–17, shows contours of the instantaneous velocity field in normal direction, at time equal 100 for three different Reynold Numbers, $Re = 20$, $Re = 100$ and $Re = 1000$.

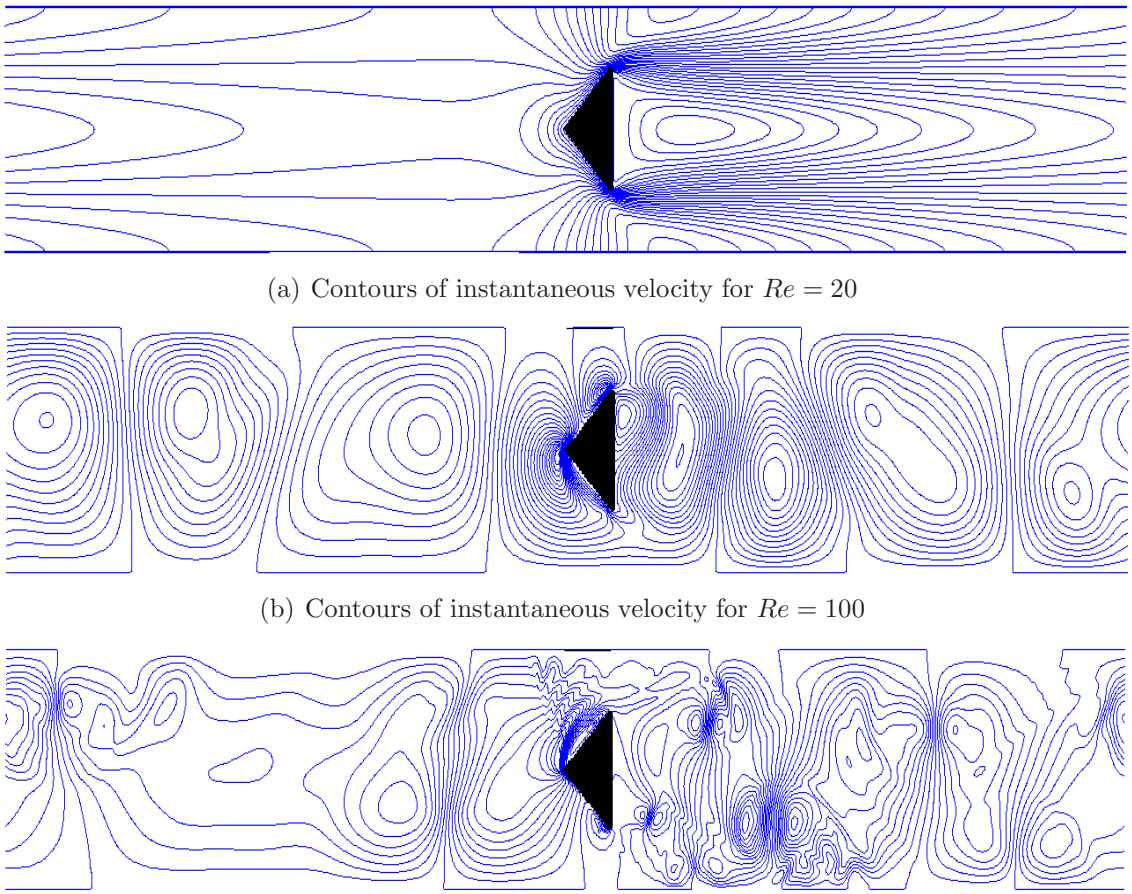

(a) Contours of instantaneous velocity for $Re = 20$

(b) Contours of instantaneous velocity for $Re = 100$

(c) Contours of instantaneous velocity for $Re = 1000$

Figure 4–17: Contours of streamwise velocity at different Re

For $Re = 20$, behind the triangular wedge there is a dificit of velocity which is gradually recovered as we move away from the body. For $Re = 100$ vortices of small scale deattach behind the flame holder and convected downstream where they become bigger and bigger. For $Re = 1000$ the structures are more complicated with small and large scale vortices mixed.

The Figure 4–18, shows the contours of the instantaneous pressure at time equal 100 for three different Reynold Numbers, $Re = 20$, $Re = 100$ and $Re = 1000$. The

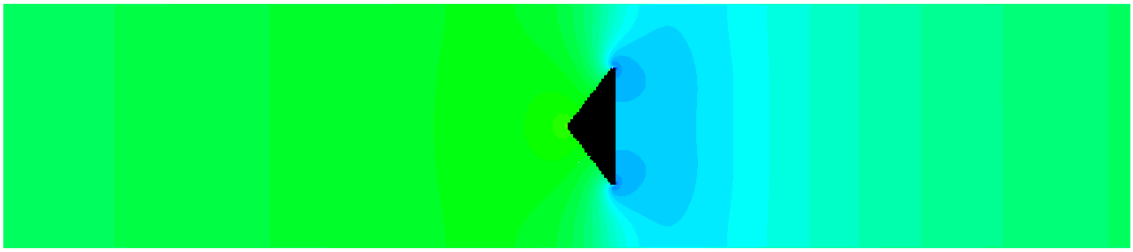

(a) Contours of pressure for $Re = 20$

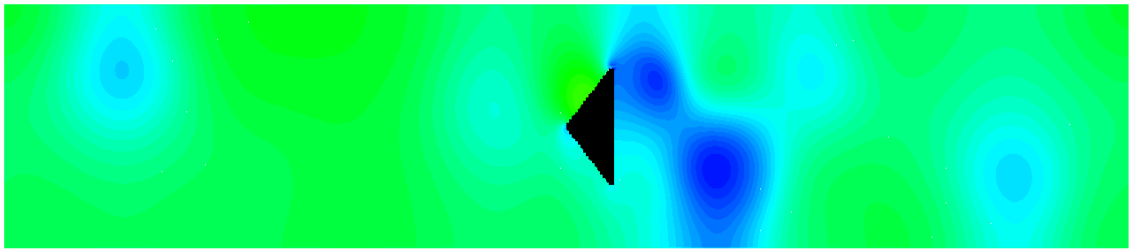

(b) Contours of pressure for for $Re = 100$

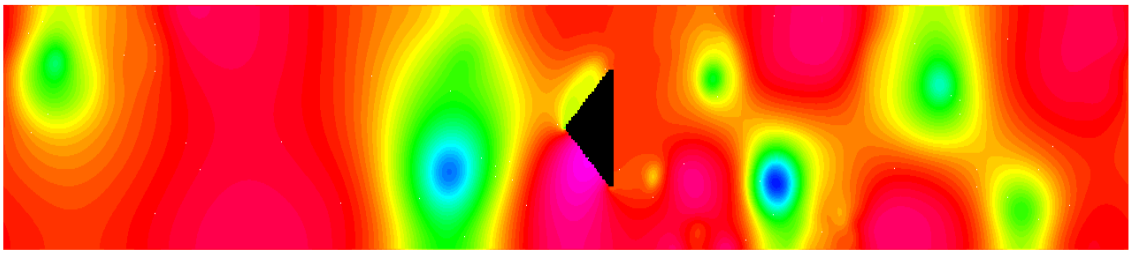

(c) Contours of instantaneous velocity for $Re = 1000$

Figure 4–18: Streamlines for different Re

pressure is uniform for $Re = 20$, symmetric with respect to the centerline. For higher Re, pressure color contours re–semble closely the voticity in the wake of the body.

The Figure 4–19 shows different stagnation points for different Reynolds Numbers, $Re = 20$, $Re = 100$ and $Re = 1000$.

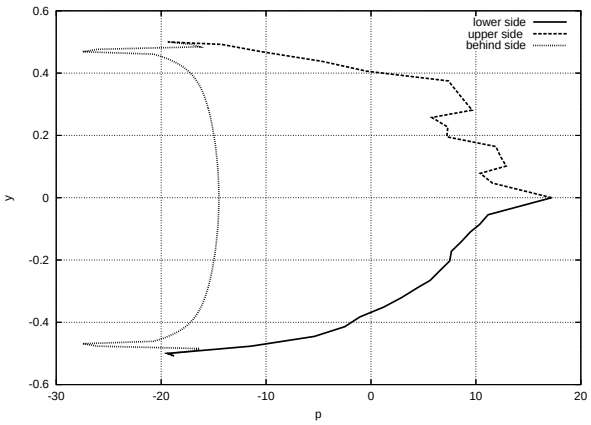

(a) Pressure profile for $Re = 20$

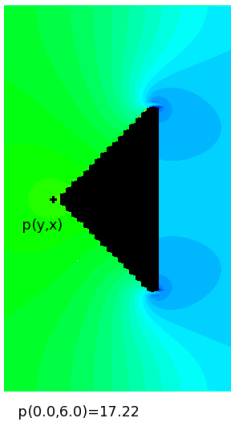

(b) Stagnation point, $Re = 20$

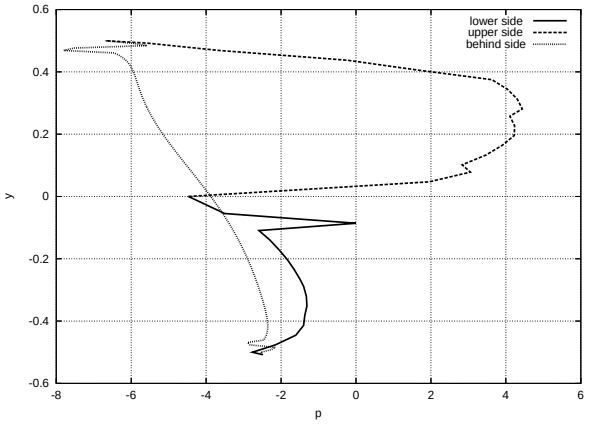

(c) Pressure profile for $Re = 100$

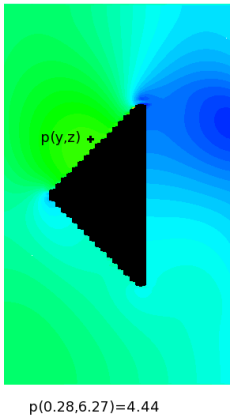

(d) Stagnation point, $Re = 100$

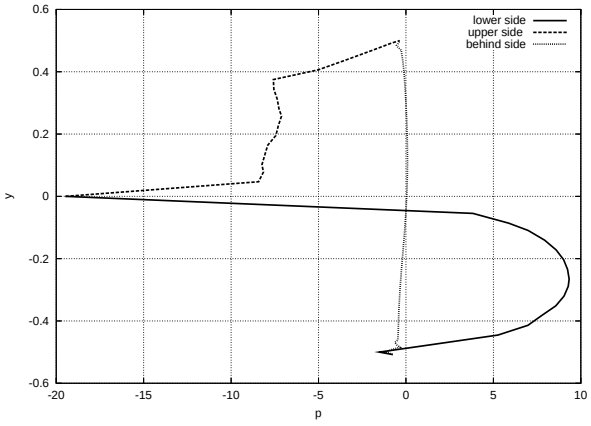

(e) Pressure profile for $Re = 1000$

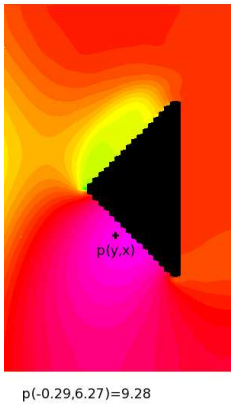

(f) Stagnation point, $Re = 1000$

Figure 4–19: Stagnation points for different Re

For $Re = 20$ the stagnation point is approximately at the center of the body. For higher Re, it moves up and down as shown in the Fig. 4–19.

4.3.2 Time dependence at $Re = 100$

Figure 4–20 shows the contours of at different times. The flow at the initial condition is symmetric and parallel. Disturbance in the flow is produces by the body. The disturbance generates unsteady wakes downstream of body along of the channel. As the flow properties of inflow and outflow are the same, by the periodicity condition, the flow upstream is no parallel but the streamlines are wavy.

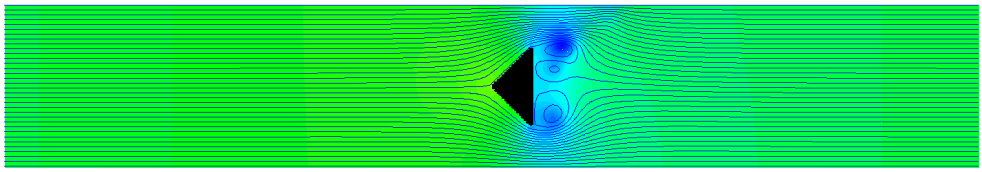

(a) $t = 0$

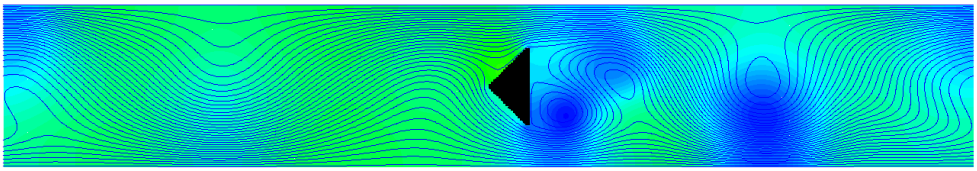

(b) $t = 55$

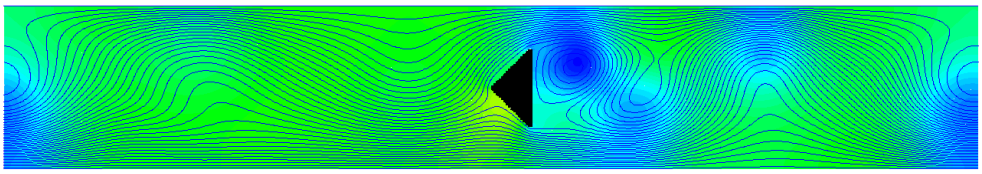

(c) $t = 65$

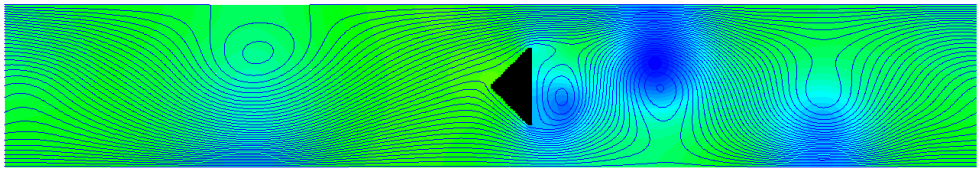

(d) $t = 80$

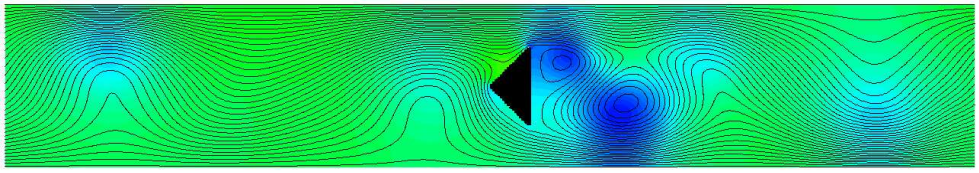

(e) $t = 100$

Figure 4–20: Contour of velocity and pressure

The Figure 4–21 shows the behavior of the pressure in the stagnation point from $t = 0$ to $t = 100$. The maximum value of the pressure in the stagnation point is, $p(y, x) = 4.953182$, corresponding to $y = -0.1640625$ and $x = 6.15$ at the time $t = 65$.

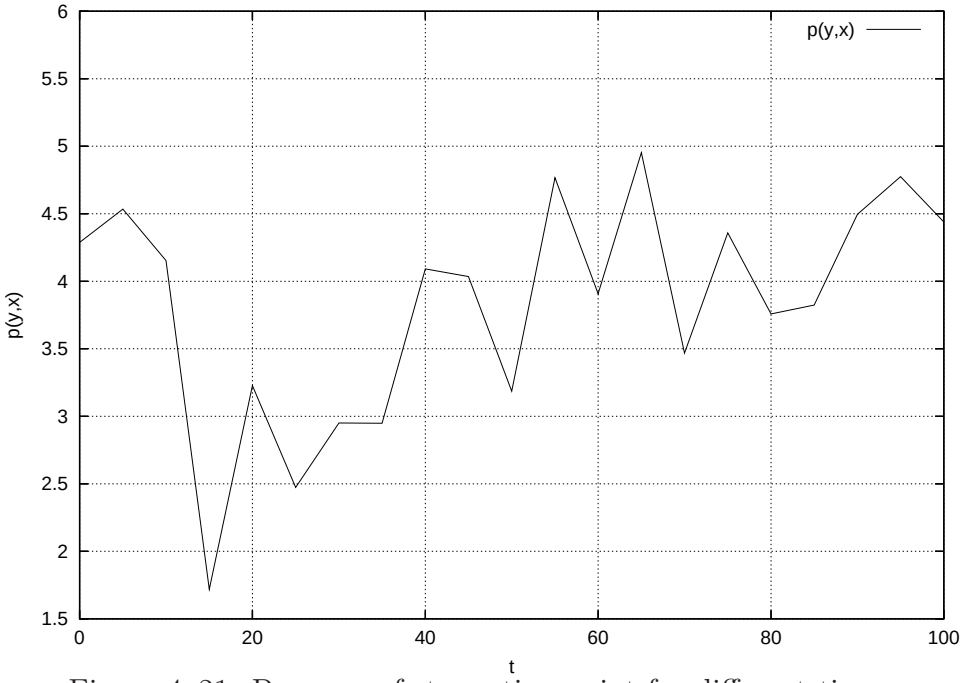

Figure 4–21: Pressure of stagnation point for different times

The Figure 4–22 shows the variation of the of the position of the stagnation point in time $t = 0$ to $t = 100$. Data are not continues but velocity fields were saved every 5 times units. Before $t = 10$, the stagnation point is placedat the centerline of the channel flow. After $t = 10$ the stagnation point oscilates between top and bottom of the body (note that $y = 0$ corresponds to the centerline of the channel).

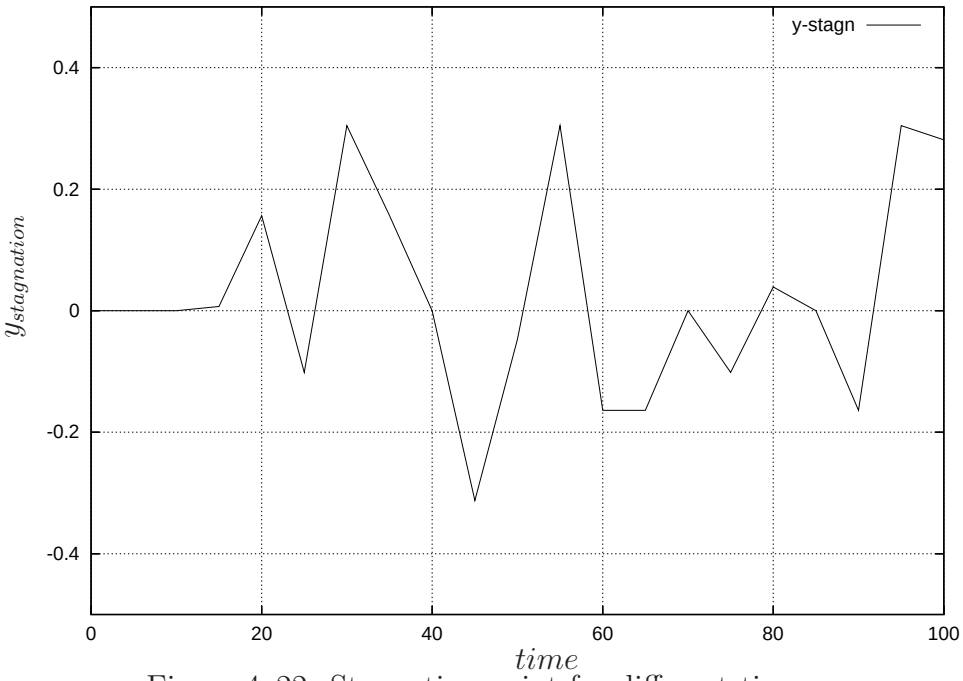

Figure 4–22: Stagnation point for different times

CHAPTER 5
3D FLOW OVER A TRIANGULAR FLAMEHOLDER

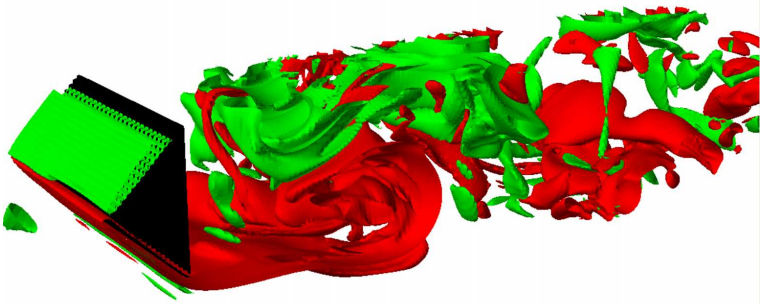

Figure 5–1: Iso-surface of instantaneous spanwise vorticity for $Re = 2000$: green positive ($\omega_z = 5$), red negative ($\omega_z = 5$).

A direct numerical simulation of the three dimensional flow over the triangular flameholder has been performed. The computational box is $12hx2hx4h$ in the streamwise, normal wall and spanwise direction respectively. The grid is $400x256x128$. Three simulations at three different Reynolds numers have been carried out $Re = 1000, 2000, 3000$. The geometrical set up is the same as that for 2D simulations, however, solving the three dimensional Navier Stokes equations allows the dynamics of vorticity to be solved. In particular the vortex stretching and vortex tilting cannot be solved in a 2D computational box. In fact in Fig. 5–1 the vortex dynamic differs from that in a 2D simulation. Vortex sheets are formed on the front faces of the flameholder. The sign of the vorticity is opposite on the two front faces of the body since part of the fluid is deviated upward, the other downward. The sheets of vorticity are convected dowstream, and roll alternatively in spanwise vortices. The spanwise vortex structures interact with the sheets of vorticity determining the

alternative deattachment of the vortex sheets from the vertical side of the flameholder. The mechanism appears similar to the generation of a Karman wake behind a cylinder.

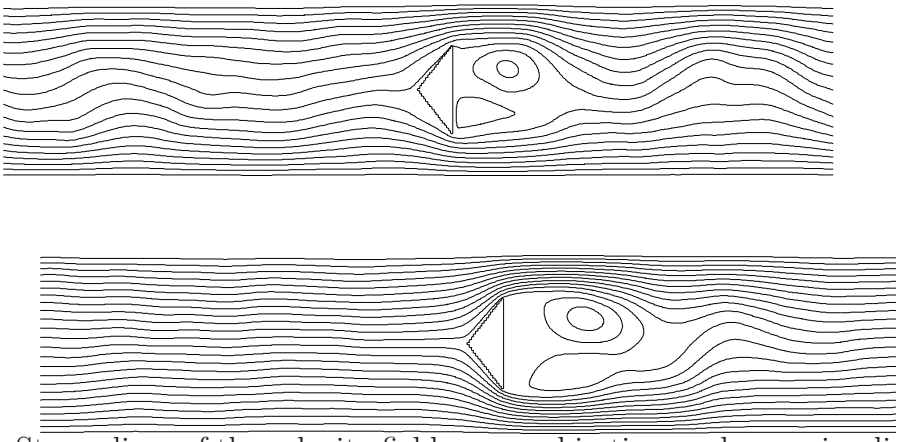

Figure 5–2: Streamlines of the velocity field averaged in time and spanwise direction for $Re = 1000$ (top) and $Re = 2000$ (bottom).

The streamlines of the flow averaged in time and spanwise direction are shown in Fig.5–2. Averaging in the spanwise direction and time, the wavyness almost disappears. With more velocity fields the averaged streamlines should be symmetric.

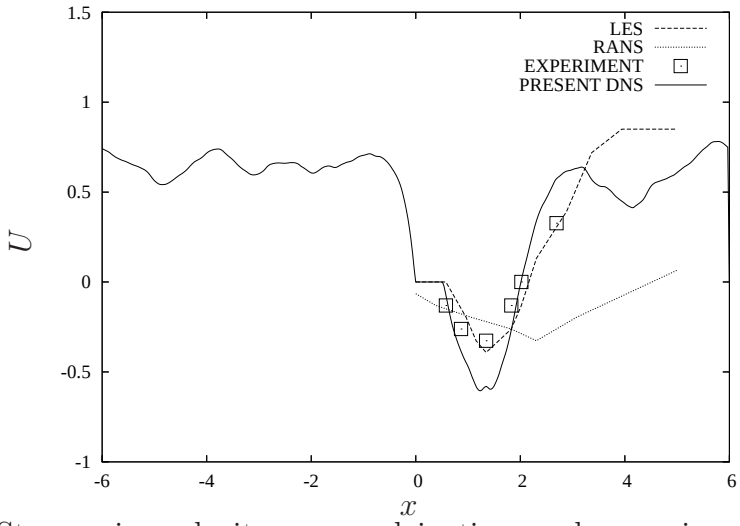

Figure 5–3: Streamwise velocity averaged in time and spanwise direction at the centerline of the channel. LES, RANS and experiments are from Kim *et al.* 2006.

To measure the extent of the recirculation region, the streamwise velocity averaged in time and spanwise direction has been plotted at the centerline of the channel (Fig.5–3). The velocity upstream the flameholder is about $U = 0.85$ and it is zero at

the stagnation point on the body. In the wake of the body (for x/h¿6.5), the velocity is negative as a result of the recirculations observed in Fig.5–2. At the end of the recirculating region the velocity becomes positive and gradually reach the value of $U = 0.85$ as upstream of the wedge. The extent of the recirculating region (where $U < 0$) is about $2h$ and represents the zone where the combustion is stabilized. The comparison of the results with LES and experiments carried out by Kim *et al.* (2006) at UT are encouraging despite the different Reynolds number (the data were scanned, digitalised and normalised with the inflow velocity by us). The LES and experiments were performed at $Re = 400,000$ while the higher Reynolds number for the present direct numerical simulations is $Re = 3,000$. Since in a triangular body the separation points are due to discontinoities in the geometry rather than to viscosity, the Reynolds number is not significant as in other geometries (cylinder). The velocity in the recirculation region, in the present simulation is higher than that found experimentally and with LES. It is well known that experiments are approximated in the regions of reverse flow, and LES can filter high gradient of velocity. Our result, provided the low Reynolds number may be more accurate then Kim's *et al.* (2006) results. The RANS results are a very bad approximation of DNS and experiments. This shows how nowadays it is necessary that industries use more refined numerical tools than RANS.

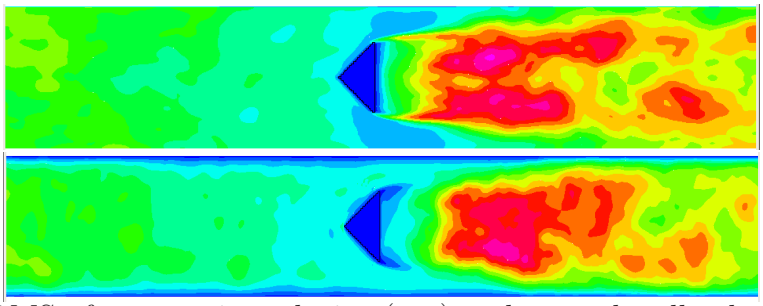

Figure 5–4: RMS of streamwise velocity (top) and normal wall velocity (bottom); statistics have been done in time and spanwise direction: red high, blue low.

The rms of streamwise and normal wall velocity have been computed with respect to the mean velocity field averaged in time and spanwise direction. The

color countours of rms are shown in Fig. 5–4. In the wake of the flameholder high values of U_{rms} and V_{rms} are observed. This region of high fluctuations corresponds to the recirculation (see Fig.5–2 for reference). In fact, this is the region where there is vortex shedding from the bluff body. Moving away from the flameholder, the vorticity becomes weaker and as a consequence the fluctuations of velocity and the rms values decrease.

CHAPTER 6
CONCLUSIONS

On a general level, we believe that the present results demonstrate the potentiality of direct numerical simulations for providing reliable information on the structure and underlying mechanisms of turbulence on bluff body. Specifically, useful results have been obtained for a fully developed turbulent channel flow with a smooth upper wall and a lower wall and a bluff–body in the center the channel flow.

For different Reynold Numbers, instantaneous flow properties such as pressure and velocity are numerically calculated using direct numerical simulation. These values are visualizated throughout the contours of pressure and velocities. Comparison of the reatachment length with experiments and LES results showed good agrement despite the difference in the Reynods Numbers (3000 for the present thesis, 400000 for Kim *et. al.*). RANS is a poor aproximation of LES and DNS, therefore industries should uses more advanced tools as DNS and LES for their design.

APPENDICES

APPENDIX A
THE NUMERICAL CODE

This appendix describes in detail the functioning of the Navier Stoke's solver.

A.1 Main

This is the main program from which all other subroutines are called. It also opens the most important data file *wavy.d*. This contains all of the parameters of the flow, the most important of which are described below.

- (n1,n2,n3) Number of grid points in each of the three orthoganal directions.
- (nsst) The integration scheme to be used in time. (nsst=1 Adam Bashfort, nsst=3 Runge-Kutta)
- (nwrit) Desribes if certain data files will be written, usually set to 1.
- (nread) If a run is being continued, this must be set to 1. The program will then initiate from a previously written *field.dat* file, and will not induce a white noise disturbance throughout the flow.
- (alx3,alx1) These are scaling factors for the domain in the directions x_3 and x_1 respectively. The exact domain size is the factor multiplied by π.
- (str2,istr2) These are parameters describing the distortion of the mesh, used to increase the density of points in the near wall region. *istr2* is an integer describing the type of channel, while *str2* describes the distortion within that channel.
- (Re) Reynold's number of the flow.
- (vper) This acts as a scaling factor for the initial random white noise disturbance, usually equal to 10^{-3}.

- (icfl,cflc,dt) If $icfl = 1$ then the code imposes the condition that $CFL = cflc = const$, otherwise the condition $\Delta t = dt = const$ is used.
- (tprin,tfin) *tfin* is the finishing time of the simulation. *tprin* is the time interval at which the entire field is written, along with files containing other data such as velocity rms values.
- (uosc,ichan) *ichan* determines whether the flow is a Poiseuille (=1) or Couette (=0) distribution in the x_2 direction. The variable *uosc* must be set to 1 for Couette to force a slip condition on the upper wall in the streamwise direction.
- (flowq2l,flowq2u,phase) The first two parameters act as scaling factors for the sinusoidal distributions of transpiration flow through the lower and upper walls respectively. *phase* $(*\pi)$ is the phase difference, in the streamwise direction, between the distribution on the upper surface and that of the lower.
- (alph,amu) These parameters define the wave number of the transpiration distribution, and therefore must be carefully set to ensure only complete waves are included in the domain. Otherwise a discontinuity may occur in the periodicity between opposite walls in the computational space. *alph* acts in the streamwise direction, whilst *amu* is in the spanwise.

A.2 Initialisation

Openfi

This sub-routine opens all of the files to be read from and written to. The varables of interest are recorded to memory.

Solve

This subroutine acts as the root of the program, calling all subroutines in order, depending on the conditions, as defined in the data file *wavy.d*.

Meshes

This subroutine calculates the size of the mesh steps in each of the three orthogonal directions, their inverses, and the squar of their inverses. It takes into account the size of the domain and the number of mesh points, i.e.

$$d1x1 = \frac{alx1}{float(n1m)}$$

Indic

In this subroutine a set of six matrices of indices are calculated. A +1 and a -1 for each orthogonal direction. These allow the program to wrap around the periodic conditions from one wall to the opposite.

Coordi

This subroutine maps the physical field onto the computational domain. It takes account of the stretch and number of mesh points defined in *wavy.d*. The computational domain may be considered to be uniform, in integer steps, since it is the physical field which undergoes distortion.

The channel type is also defined by the variable *istr2* as follows:

0	standard channel	4	wavy channel
1	modified channel	5	wavy channel, $a = 0.5$
2	new groove	6	floryan test case
3	morrison channel	7	roughness

Sensore

This is an optional subroutine which calculates the position in x_3 of probes to measure the point's time history. It also opens the files to which this information will be written.

Body

This subroutine is only important in the case where a physical body is immersed in the flow, i.e. a roughness element or wavyness element. It works in combination with three further subroutines (*gebody*, *geomety3* and *geometry2*). They primarily

locate points which are lying within the body, and those on or close to the external perimeter.

Metric

This subroutine calculates the metric quantity, $\frac{d\xi}{dx}$, used to define the transformation between the computational space, $x = f(\xi)$, where $0 \leq \xi \leq 1$ to physical space, $0 \leq x \leq alx_i$.

$$\frac{\partial u}{\partial x} = \frac{\partial u}{\partial \xi}\frac{d\xi}{dx}$$

Initia

This subroutine defines the initial conditions throughout the computational domain.

Outh

This subroutine writes parameter values which are to be considered over time. Usually written much more often than the `field.dat` files, the following values are recorded. The time interval is dependent on either *tpin* or *tprin* depending on whether *dt* is constant.

- Iterative step
- Time
- Average velocity in three directions
- Pressure gradient
- Turbulent energy
- CFL

Phini

In the second chapter the method for solving the pressure term was described, requiring the equation below to be solved

$$\nabla \cdot \nabla \psi = div\hat{q}$$

This subroutine prepares the coefficients of the discretisation in space of $\nabla \cdot \nabla \psi$.

Coeinv

The coefficients for the disceretisation of the terms for the second derivative are calculated in this subroutine.

A.3 Time Iteration

The following subroutines are run in a continuous cycle, once for each time step. The looped is exited when the condition $time \geq tfin$ is satisfied.

CFL

This subroutine calculates *dt* based on the imposed value of CFL (*cflc*) defined in *wavy.d*. The subroutine is only called if the condition $icfl = 1$ is satisfied. If not, then the value of *dt* used, will be that defined in *wavy.d*. Checks are made on the calculated value of *dt* to ensure it is between certain limits. The CFL parameter is evaluated by solving the following equation:

$$\left(\frac{\Delta x}{q}\right) * CFL = \delta t$$

Tschem

This subroutine controls the integration of the the Navier-Stokes equations by calling the following:

$Hdnl_i$

This subroutine calculates the non-linear terms in each of the three orthogonal directions. It is called three times in a loop, solving direction 'i' on each pass.

$Invtr_i$

This calculates the viscous term of the equation in the direction 'i', imposing the condition of constant mass flux. This creates a sparse matrix which can be equated as the sum of three diagonal matrices. The result of this gives us the required value $\hat{q}$.

Divg

Calculates the divergence of the velocity field.

Phcalc

The following equation is solved:

$$\nabla \cdot \nabla \psi = div\hat{q}$$

Updvp

Solves the equation below to find the velocity field throughout the entire field.

$$q_i^{n+1} = \hat{q}_i - \Delta t \frac{\delta \psi}{\delta x_i}$$

Prcalc

Calculate the pressure field at the new time point.

Enerca

This calculates the energy, vorticity, stream function and velocity at every node.

Divgck

This subroutine carries out the check for divergence, by calculating the global divergence. The condition to be met is shown below: $\text{div} < 0.2 * 10^{-3}$

Contwr

This subroutine writes the `field.dat` files, and several other files containing statistics about the flow every time step in which both the following two conditions are met:

$$MOD(\text{nprint,ntime}) = 0$$

$$\text{nwrit} = 1$$

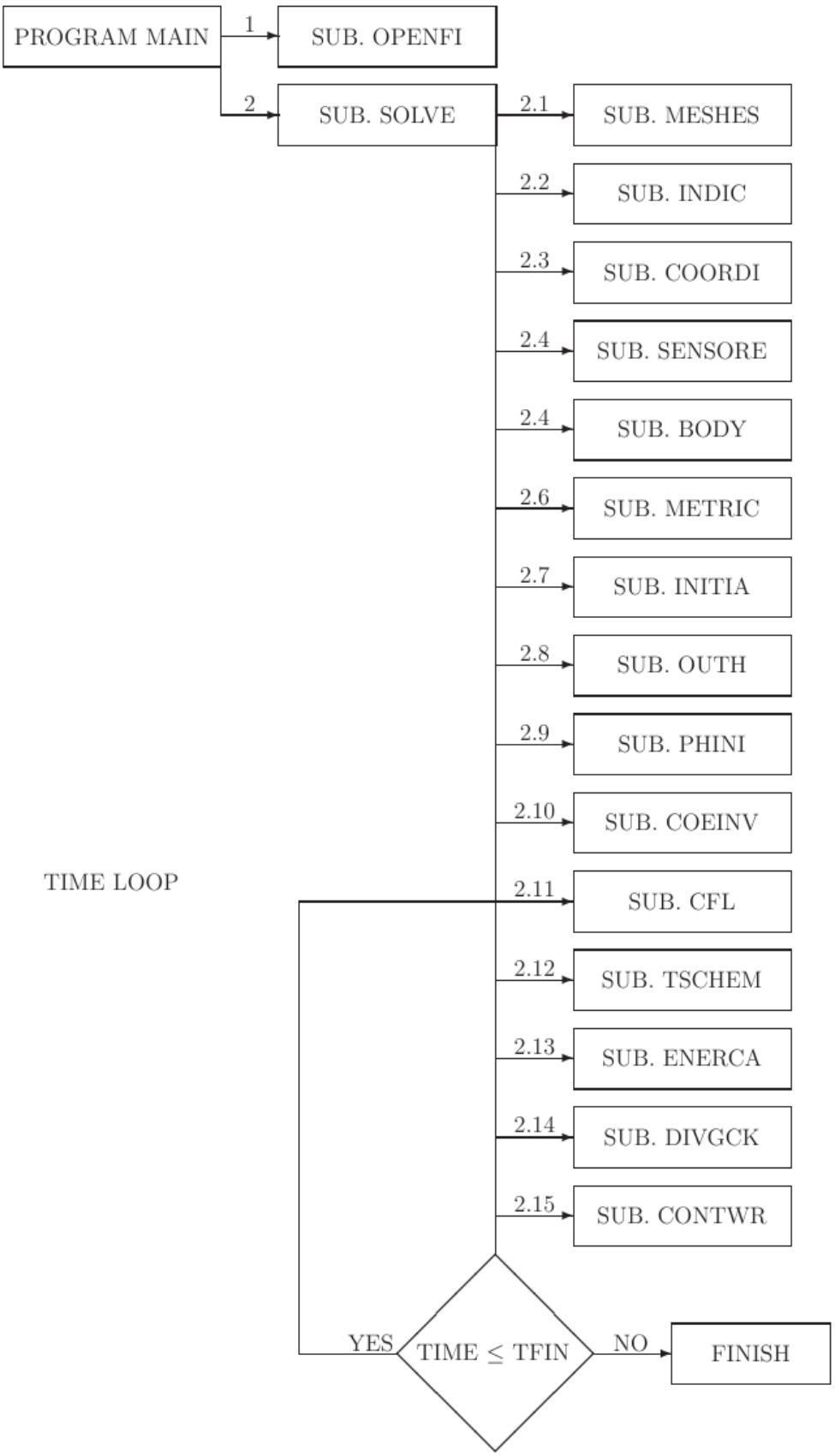
PROGRAM MAIN
1
SUB. OPENFI
2
SUB. SOLVE
2.1
SUB. MESHES
2.2
SUB. INDIC
2.3
SUB. COORDI
2.4
SUB. SENSORE
2.4
SUB. BODY
2.6
SUB. METRIC
2.7
SUB. INITIA
2.8
SUB. OUTH
2.9
SUB. PHINI
2.10
SUB. COEINV
TIME LOOP
2.11
SUB. CFL
2.12
SUB. TSCHEM
2.13
SUB. ENERCA
2.14
SUB. DIVGCK
2.15
SUB. CONTWR
YES
TIME ≤ TFIN
NO
FINISH

APPENDIX B
POST PROCESSSING

```
c      ****************************************************************
c      Date: 01/02/2008 - IV semester
c      ****************************************************************
       program average
       parameter(n=3,m1=100,m2=300,m3=500)
       dimension q(n,m1,m2,m3),pr(m1,m2,m3)
       dimension vca(n,m2,m3),sigma(n,m2,m3)
       real*4 vcasin(n,m2,m3)
       real*4 sigmasin(n,m2,m3)
       dimension yp1(m1),yp2(m2),yp3(m3)
       real*4 yp1sin(m1),yp2sin(m2),yp3sin(m3)
       dimension forclo(n,m2,m3)
       real*4 forclosin(n,m2,m3)
       real*4 q1(n,m2,m3)
       character(len=3) kpfi

       nfil=15
       open(nfil,file='../field0020.dat',form='unformatted')
```

```
      read(nfil)n1m,n2,n3m
      write(*,*) n1m,n2,n3m
c          48         257         400

      read(nfil)ntime,time,ene0,dp3ns,enav,cfn,dt
c      write(*,*)ntime,time,ene0,dp3ns,enav,cfn,dt
      read(nfil)
     1           (((q(1,i,j,k),i=1,n1m),j=1,n2),k=1,n3m),
     1           (((q(3,i,j,k),i=1,n1m),j=1,n2),k=1,n3m),
     1           (((pr(i,j,k) ,i=1,n1m),j=1,n2),k=1,n3m)
      close(nfil)

      open(44,file='q3i.plo')
      do i=1,n1m
        write(44,*)i, q(3,i,50,50)
      enddo
      close(44)


      open(99,file='../xgrid.plo')
      do i=1,n1m
        read(99,*) m, yp1(i)
c        read(99,*) dum
        write(33,*) m, yp1(i)
        yp1sin(i)=yp1(i)
      enddo
      close(99)
```

```
      open(100,file='../ygrid.plo')
      do j=1,n2
        read(100,*) m, yp2(j)
        read(100,*) dum
        write(34,*) m, yp2(j)
        yp2sin(j)= yp2(j)
      enddo
      close(100)


      open(101,file='../zgrid.plo')
      do k=1,n3m
        read(101,*) m, yp3(k)
c        read(101,*) dum
        write(35,*) m, yp3(k)
        yp3sin(k)= yp3(k)
      enddo
      close(101)


c     ***************************
c     normal velicity on the wall
c     ***************************

      do k=1,n3m
         do i=1,n1m
```

```
            q(2,i,1,k)=0.
            do j=1,n2
               sucai=1./(yp1(i+1)-yp1(i))
               sucaj=1./(yp2(j+1)-yp2(j))
               sucak=1./(yp3(k+1)-yp3(k))
               dqcap=(q(1,i+1,j,k)-q(1,i,j,k))*sucai
     1         +(q(3,i,j,k+1)-q(3,i,j,k))*sucak
               q(2,i,j+1,k)=q(2,i,j,k)-dqcap/sucaj
            enddo
         enddo
       enddo

       open(102,file='q2.plo')
       do j=1,n2
         write(102,*) yp2(j),q(2,1,j,100)
       enddo
       close(102)



c      ************************************************
c      Average_i
c      ************************************************

       do k=1,n3m
         do j=1,n2
           vca(2,j,k)=0.
           vca(3,j,k)=0.
```

```
          do i=1,n1m
            vca(2,j,k)=vca(2,j,k)+q(2,i,j,k)
            vca(3,j,k)=vca(3,j,k)+q(3,i,j,k)
          enddo
            vca(2,j,k)=vca(2,j,k)/n1m
            vca(3,j,k)=vca(3,j,k)/n1m
        enddo
      enddo

      open(103,file='vca2.plo')
      do j=1,n2
         write(103,*) yp2(j), vca(2,j,100)
      enddo
      close(103)




c     ******************************************************
c     RMS
c     ******************************************************

      do k=1,n3m
        do j=1,n2
          sigma(2,j,k)=0.
          sigma(3,j,k)=0.
          do i=1,n1m
            sigma(2,j,k)=sigma(2,j,k)+(q(2,i,j,k)-vca(2,j,k))**2
```

```
            sigma(3,j,k)=sigma(3,j,k)+(q(3,i,j,k)-vca(3,j,k))**2
          enddo
            sigma(2,j,k)=sigma(2,j,k)/n1m
            sigma(3,j,k)=sigma(3,j,k)/n1m
        enddo
      enddo

      do k=1,n3m
         do j=1,n2
           sigma(2,j,k)=(sigma(2,j,k))**(0.5)
           sigma(3,j,k)=(sigma(3,j,k))**(0.5)
         enddo
      enddo

      open(104,file='sigma2.plo')
      do j=1,n2
        write(104,*) yp2(j),sigma(2,j,100)
      enddo
      close(104)

c     ****************************************************************
c     Average and rms for any sections
c     ****************************************************************

      write(*,*) 'Give me the k section'
      read(*,*) kk
      write(kpfi,100)kk
```

```
100   format(i3.3)
      open(105,file='../average/vca2sec_'//kpfi//'.plo')
      do j=1,n2
         write(105,*) yp2(j),vca(2,j,kk)
      enddo
      close(105)

      open(106,file='../average/vca3sec_'//kpfi//'.plo')
      do j=1,n2
         write(106,*) yp2(j),vca(3,j,kk)
      enddo
      close(106)

      open(107,file='../rms/sigma2sec_'//kpfi//'.plo')
      do j=1,n2
         write(107,*) yp2(j),sigma(2,j,kk)
      enddo
      close(107)

      open(108,file='../rms/sigma3sec_'//kpfi//'.plo')
      do j=1,n2
         write(108,*) yp2(j),sigma(3,j,kk)
      enddo
      close(108)


      write(*,*) 'Give me the j section'
```

```
      read(*,*) jj
      write(kpfi,101)jj
101   format(i3.3)
      open(109,file='../rms/sigma2sec_'//kpfi//'.plo')
      do k=1,n3m
         write(109,*) yp3(k),sigma(2,jj,k)
      enddo
      close(109)

      open(110,file='../rms/sigma3sec_'//kpfi//'.plo')
      do k=1,n3m
         write(110,*) yp3(k),sigma(3,jj,k)
      enddo
      close(110)

c     ********************************************************
c     Turb3d-rms
c     ********************************************************

      open(111,file='../dat_plo/cord2drms.dat')
      rewind 111
      write(111,*) n2,n3m
      write(111,*)
     1            ((yp2sin(j),j=1,n2),k=1,n3m),
     1            ((yp3sin(k),j=1,n2),k=1,n3m)
      close(111)
```

```
  open(112,file='../forclo.dat')
  read(112,*) n2,n3
  write(*,*) n2, n3
  read(112,*) epsil,lamb,re,time
  read(112,*)
1           ((forclo(1,j,k), j = 1, n2), k= 1, n3)
1          ,((forclo(2,j,k), j = 1, n2), k= 1, n3)
1          ,((forclo(3,j,k), j = 1, n2), k= 1, n3)

  do k=1,n3
     do j=1,n2
        forclosin(1,j,k)=forclo(1,j,k)
        forclosin(2,j,k)=forclo(2,j,k)
        forclosin(3,j,k)=forclo(3,j,k)
     enddo
  enddo
  close(112)

  open(44,file='../dat_plo/forclo.dat')
  write(44,*) n2,n3
  write(44,*) epsil,lamb,re,time
  write(44,*)
1           ((forclo(2,j,k), j = 1, n2), k= 1, n3)
1          ,((forclo(3,j,k), j = 1, n2), k= 1, n3)
1          ,((forclo(3,j,k), j = 1, n2), k= 1, n3)
  close(44)
```

```
c       open(55,file='../dat_plo/intercepto.plo')
c       do k=1,n3
c        do j=1,n2
c           if (forclo(2,j,k)==1.0) write(55,*) j,k
c        enddo
c       enddo
c       close(55)


       open(113,file='../dat_plo/forclorms.dat')
       write(113,*)n2,n3m
       write(113,*) epsil,lamb,re,time
       write(113,*)
     1           ((forclosin(2,j,k), j = 1, n2), k= 1, n3m)
     1          ,((forclosin(3,j,k), j = 1, n2), k= 1, n3m)
     1          ,((forclosin(3,j,k), j = 1, n2), k= 1, n3m)
     1          ,((1., j = 1, n2), k= 1, n3m)
       close(113)


      do k=1,n3m
        do j=1,n2
          q1(2,j,k)=q(2,1,j,k)
          q1(3,j,k)=q(3,1,j,k)
        enddo
      enddo
```

```
 nfil=18
 eps=100
 open(nfil,file='../dat_plo/instant.dat')
 write(nfil,*)n2,n3m
 write(nfil,*) eps,eps,eps,eps,eps
 write(nfil,*)
1            ((q1(2,j,k),j=1,n2),k=1,n3m),
1            ((q1(3,j,k),j=1,n2),k=1,n3m),
1            ((q1(2,j,k),j=1,n2),k=1,n3m),
1            ((q1(3,j,k),j=1,n2),k=1,n3m)
  close(nfil)


  do k=1,n3m
    do j=1,n2
      vcasin(2,j,k)=vca(2,j,k)
      vcasin(3,j,k)=vca(3,j,k)
    enddo
  enddo

  nfil=16
  eps=100
  open(nfil,file='../dat_plo/vcauv.dat')
  write(nfil,*)n2,n3m
  write(nfil,*) eps,eps,eps,eps
  write(nfil,*)
```

```
1            ((vcasin(2,j,k),j=1,n2),k=1,n3m),
1            ((vcasin(3,j,k),j=1,n2),k=1,n3m),
1            ((vcasin(2,j,k),j=1,n2),k=1,n3m),
1            ((vcasin(3,j,k),j=1,n2),k=1,n3m)
  close(nfil)

  do k=1,n3m
    do j=1,n2
      sigmasin(2,j,k)=sigma(2,j,k)
      sigmasin(3,j,k)=sigma(3,j,k)
    enddo
  enddo

  nfil=17
  eps=100
  open(nfil,file='../dat_plo/rmsuv.dat')
  write(nfil,*)n2,n3m
  write(nfil,*) eps,eps,eps,eps
  write(nfil,*)
1            ((sigmasin(2,j,k),j=1,n2),k=1,n3m),
1            ((sigmasin(3,j,k),j=1,n2),k=1,n3m),
1            ((sigmasin(2,j,k),j=1,n2),k=1,n3m),
1            ((sigmasin(3,j,k),j=1,n2),k=1,n3m)
  close(nfil)



  end
```

REFERENCE LIST

[1] INTEGOVERNMENTAL PANEL ON CLIMATE CHANGE. Climate Change and Biodiversity. *IPCC*, **V**:55, 2002.

[2] Kim, W., Lianau, J. J., Van S. P., Colket III P. R., Malecki R. E. & Syed, S. Toward Modeling Lean Blow Out in Gas Turbine Flameholder Applications. *International Gas Turbine Institute of ASME*, **128**:40–48, Jan 2006.

[3] Raffoul, C. N., Nejad, A. S. & Gould, R. D. Three–component velocity measurements downstream of a bluff–body flameholder. *AERO PROPULSION AND POWER DIRECTORATE WRIGHT LABORATORY AIR FORCE MATERIAL COMMAND*, 1995.

[4] Lefebvre, A. H. Gas Turbine Combustion. *MacGraw–Hill.*

[5] Longwell, J. P., Frost, E. E. & Weiss, M. A. Flame Stability in Bluff Body Recirculation Zones. *Stanford Oil Development Co.*

[6] Prasad, A. & Williamson, C. Three–dimensional effects in turbulent bluff–body wakes. *Journal of Fluid Mechanics*, **343**:235–265, 1997.

[7] Johansson, S. & Davidson, L. Calculation of the Unsteady Turbulent Flow behind a Triangular Flameholder *CERFACS*, 1991.

[8] Fuji, S., Gomi, M. & Eguchi, K. Cold Flow Tests of Bluff–Body Flame Stabilizer. *Journal of Fluids Engineering*, **100**:323–332, 1978.

[9] Hoffman, J. & Johnson, C., Computational Turbulent Incompressible Flow, *Springer*, first edition, 2007,

[10] CHUNG, T. J. COMPUTATIONAL FLUID DYNAMICS, *The Press Syndicate of the Univirsity of Cambridge*, first edition, 2002.

[11] Yeh, H. & Cummins, H. Z. Localized fluid flow measurements with He–Ne laser spectrometer. *Applied Physics Letters*, **4**:176, 1964.

[12] Lumley, L. & George, W. K. The laser–Doppler velocimeter and its application to the measurement of turbulence. *Journal of Fluid Mechanics*, **60**:321–362, 1973.

[13] Hyun, B–S., Balachandar, R., Yu, K. & Patel, V. C. PIV/LDV Measurements of Mean Velocity and Turbulence in a Complex Open Channel Flow. *IIHR–Hydroscience & Engineering*, The University of Iowa, 2003.

[14] Davidson, P. A. Turbulence an Introduction for scientists and engineers. *OXFORD University Press*, first edition, 2004.

[15] Orszag, Steven A. & Patterson, G. S. Numerical Simulation of Three-Dimensional Homogeneous Isotropic Turbulence. *Phys. Rev. Lett.*, **28**:76–79, Jan 1972.

[16] Rogallo, R.S & Moin, P. Numerical Simulation of turbulent flows *Journal of Fluid Mechanics*, **16**:99–137, 1981.

[17] Parviz, M. & Krishnan, M. DIRECT NUMERICAL SIMULATION: A Tool in Turbulence Research. *Journal of Fluid Mechanics*, **30**: 358-378, 1998.

[18] Krajnovic, S. & Davidson, L. Flow Around A Three–Dimensional Bluff Body *9TH INTERNATIONAL SYMPOSIUM ON FLOW VISUALIZATION*, **177**: 1–10, 2000.

[19] Burattini, P., Leonardi, S., Orlandi, P. & Antonia, R. A. Comparison between experiments and direct numerical simulation in a channel flow with roughness on one wall. *Journal of Fluid Mechanics*, 2007.

[20] Hanjalic, K. & Launder, B. E. Fully developed assymmetric flow in a plane channel. *Journal of Fluid Mechanics*, **51**:301–335, 1972.

[21] Ikeda, T. & Durbin, P. A. Direct Simulation of a Rough Wall Channel Flow. *Stanfor University*, 2002.

[22] Leonardi, S., Tessicini, F., Orlandi, P. & Antonia R. A. Direct Numerical and Large–Eddy Simulation of Turbulent Flows over Rough Surface. *AIAA Journal* **44**:2482–2487, 2006.

[23] Leonardi, S., Djenidi, L., Orlandi, P. & Antonia, R. A. Guidelines for Modeling a 2D Rough Wall Channel Flow *Turb, Flow & Comb.*, **77**:41–57, 2006.

[24] Orlandi, P. Fluid Flow Phenomena : A Numerical Toolkit. *Dordrecht, Kluwer*, first edition, 2000.

[25] Fadlun, E. A., Verzicco, R., Orlandi, P. & Mohd–Yusof, J. Combined immersed boundary finite–difference methods for three–dimensional complex flow simulation. *Journal of Computational Physics*, **161**:35–60, 2000.

[26] Wray, A. A. Vely low storage time–advancement schemes. *NASA Ames Research Center, Moffet Field, California: Internal Report*, 1987.

[27] Peskin, C. S. Flow patterns around heart valves: a numerical method. *J. of Com. Phys.*, **10**:252–271, 1972.

[28] Peskin, C. S. Numerical analysis of blood flow in the heart. *J. of Com. Phys.*, **25**:220–252, 1977.

[29] McQueen, D. M. & Peskin, C. S. Shared-memory parallel vector implementation of the immersed boundary method for the computation of blood flow in the beating mammalian heart. *J. of Supercomp.*, **11**:213–236, 1997.

[30] McQueen, D. M. & Peskin, C. S. A three–dimensional computational method for blood flow in the heart. II. Contractile fibers. *J. of Comp. Phys.*, **82**:289–297, 1989.

[31] Briscolini, M. & Santangelo, P. Development of the mask method for incompressible unsteady flows *J. of Comp. Phys.*, **84**:57–75, 1989.

[32] Goldstein, D., Handler, R. & Sirovish, L. Modeling a no–slip flow boundary with an external force field. *J. of Comp. Phys.*, **105**:354–366, 1993.

[33] Saiki, E. M & Biringen, S. Numerical simulation of a cylinder in uniform flow: application of a virtual boundary method... *J. of Comp. Phys.*, **123**:405–465, 1996.

[34] Goldstein, D., Handler, R. & Sirovich, L. Modeling a no–slip flow boundary with an external force field. *Journal of Fluid Mechanics*, **302**:333–375, 1995.

[35] Goldstein, D. & Tuan, T. C. Secondary flow induced by riblets. *Journal of Fluid Mechanics* **363**:115–151, 1998.

[36] Saiki, E. M. & Biringen, S. Spatial numerical simulation of boundary layer transition:effects of a spherical particle. *Journal of Fluid Mechanics*, **345**:133–164, 1997.

[37] Arthurs, K. M., Moore, L. C. & Peskin, C. Modeling arteriolar flow and mass transport using the immersed boundary method. *J. of Comp. Phys.*, **147**:405–465, 1998.

[38] Mohd–Yusof, J. Combined Immersed boundaries/B–splines methods for simulations of flows in complex geometries. *CTR Annual Research Briefs 1997, NASA Ames/Stanford Univ.*, 1997.

[39] Cherukat, P., Na, Y., Hanratty, T. J. & McLaughlin, J. B. Direct numerical simulation of a fully developed turbulent flow over a wavy wall. *Theoret. Comput. Fluid Dynamics*, **11**:109–134, 1998.

[40] Hudson, J. D. The effect of a wavy boundary on turbulent flow. *PhD thesis, University of Illinois, Urbana*, 1993.

[41] Buckles, J., Hanratty, T. J. & Adrian, R. Turbulent production in flow over a wavy wall. *Exps. Fluids* **140**:27–44, 1984.

[42] Henn, D. S. & Sykes, R. I. Large–eddy simulation of flow over wavy surfaces. *Journal of Fluid Mechanics*, **383**:75–112, 1999.

[43] Kim, J. & Moint, P. Application of a fractional step method to incompressible Navier-Stoke's equations. *Journal Comp. Phys.*